

**DEVELOPMENT OF OPTICAL TOMOGRAPHY
TECHNIQUE FOR MONITORING BIOFILM
FORMATION**



**A Thesis Submitted in Partial Fulfillment of the Requirements for the
Degree of Master of Science in Applied Physics
Suranaree University of Technology
Academic Year 2018**

การพัฒนาเทคนิคโทโมกราฟฟีเชิงแสงเพื่อติดตาม
การก่อตัวของไบโอฟิล์ม



วิทยานิพนธ์นี้เป็นส่วนหนึ่งของการศึกษาตามหลักสูตรปริญญาวิทยาศาสตรมหาบัณฑิต
สาขาวิชาฟิสิกส์ประยุกต์
มหาวิทยาลัยเทคโนโลยีสุรนารี
ปีการศึกษา 2561

**DEVELOPMENT OF OPTICAL TOMOGRAPHY
TECHNIQUE FOR MONITORING BIOFILM
FORMATION**

Suranaree University of Technology has approved this thesis submitted in partial fulfillment of the requirements for a Master's Degree.

Thesis Examining Committee



(Assoc. Prof. Dr. Sirichok Jungthawan)

Chairperson



(Asst. Prof. Dr. Panomsak Meemon)

Member (Thesis Advisor)



(Prof. Dr. Joewono Widjaja)

Member



(Dr. Sukanya Tachatraiphop)

Member



(Assoc. Prof. Dr. Worawat Meevasana)



(Prof. Dr. Santi Maensiri)

Vice Rector for Academic Affairs
and Innovationalization

Dean of Institute of Science

เจษฎา แซ่เตี้ยว : การพัฒนาเทคนิคโทโมกราฟีเชิงแสงเพื่อติดตามการก่อตัวของไบโอฟิล์ม (DEVELOPMENT OF OPTICAL TOMOGRAPHY TECHNIQUE FOR MONITORING BIOFILM FORMATION) อาจารย์ที่ปรึกษา : ผู้ช่วยศาสตราจารย์ ดร.พนมศักดิ์ มีมนต์, 43 หน้า

การถ่ายภาพตัดขวางด้วยแสงเลเซอร์/ เทคนิคโทโมกราฟี/ ความสม่ำเสมอของความหนา/ ไบโอฟิล์ม

Optical coherence tomography (OCT) เป็นเทคนิคการถ่ายภาพสามมิติ ที่มีความเร็วในการถ่ายภาพสูงและให้ความละเอียดสูง นอกจากนี้ OCT ยังเป็นเทคนิคการถ่ายภาพแบบไม่รุกรานและไม่ทำลายตัวอย่าง ซึ่งสามารถถ่ายภาพตัดขวางเชิงลึกของเนื้อเยื่อชีวภาพและวัสดุโปร่งใสอื่น ๆ วิทยานิพนธ์นี้มุ่งเน้นไปที่การประยุกต์ใช้ OCT เป็นเครื่องมือตรวจสอบเพื่อทำแผนภาพการกระจายความหนาของไบโอฟิล์มซึ่งสามารถใช้ในเฝ้าติดตามการเจริญของไบโอฟิล์ม โดยนำเสนอขั้นตอนเพื่อให้ได้แผนภาพการกระจายความหนาเชิงแสงของไบโอฟิล์ม *Legionella pneumophila* ทั้งนี้ OCT สามารถให้ข้อมูลการกระจายความหนาของไบโอฟิล์ม โดยไม่ต้องนำไบโอฟิล์มออกจากกล่องเพาะเลี้ยง เทคนิคในการหาปริมาณการกระจายความหนาและความสม่ำเสมอของการเกิดไบโอฟิล์มบนพื้นผิวโลหะที่พัฒนาขึ้น จะช่วยให้สามารถสังเกตการเจริญของไบโอฟิล์มในแต่ละบริเวณ ซึ่งผลการทดลองแสดงให้เห็นว่า การเปลี่ยนแปลงของความหนาและความสม่ำเสมอของความหนาของแผ่นไบโอฟิล์มสามารถเห็นได้ชัดเจนในช่วงสัปดาห์ที่ 3 และ 4 แผนภาพการกระจายความหนาที่ได้รับจาก OCT นั้นได้รับการพิสูจน์แล้วว่าเป็นเครื่องมือที่มีประโยชน์สำหรับการเฝ้าติดตามการเจริญเติบโตของไบโอฟิล์มในระยะต่าง ๆ

สาขาวิชาฟิสิกส์
ปีการศึกษา 2561

ลายมือชื่อนักศึกษา เจษฎา แซ่เตี้ยว
ลายมือชื่ออาจารย์ที่ปรึกษา [ลายมือ]

JADSADA SAETIEW : DEVELOPMENT OF OPTICAL TOMOGRAPHY
TECHNIQUE FOR MONITORING BIOFILM FORMATION. THESIS
ADVISOR : ASST. PROF. PAMONSAK MEEMON, Ph.D. 43 PP.

OPTICAL COHERENCE TOMOGRAPHY/ OPTICAL TOMOGRAPHY/
THICKNESS UNIFORMITY/ BIOFILM

Optical coherence tomography (OCT) is a high-speed high-resolution 3D imaging technique. In addition, OCT is a non-invasive imaging technique that can provide a depth cross section image of biological tissues and other optical transparent materials. This thesis focuses on the application of OCT as an inspection tool to map the thickness distribution of biofilm, which can be used to monitor its development over time. We present the procedure to obtain optical thickness map of *Legionella pneumophila* biofilm. OCT can provide depth information of biofilms without removing them from their culture plate. A technique to quantify the thickness distribution and uniformity of the biofilm formation on metal surface has been developed. The results show that significant changes in thickness and thickness uniformity of the biofilm can be observed during week 3 and week 4. The thickness topography obtained by OCT is proven to be a useful tool for *in vivo* monitoring of the biofilm development.

School of Physics

Academic Year 2018

Student's Signature ๒๐๒๓ ๒๕๖๓

Advisor's Signature 

ACKNOWLEDGEMENTS

I would like to thank members of all LASER Laboratory, who supported my work and helped me get results of better quality.

Special mention goes to my thesis advisor Asst. Prof. Dr. Panomsak Meemon in School of Physics at Suranaree University of Technology, for support and suggestion with kindness through his knowledge and experience. He consistently allowed this paper to be my own work, but steered me in the right direction whenever he thought I needed it.

I would like to thank Mrs. Phenkhae Petchmai and all staffs at the School of Physics, for their kindly support and help.

I would also like to thank the experts who have been beside me and helped me in many problems for this research project: Sitthichoke Ritpech, Racha pongchalee, Jiraporn Sanjae and Yutana Lenaphet, and Kunakorn Palawong.

Last but not the least, I would like to thank my family: Yupin Saetiew and to Charat Saetiew for throughout writing this thesis and my life in general.

Jadsada Saetiew

CONTENTS

	Page
ABSTRACT IN THAI.....	I
ABSTRACT IN ENGLISH.....	II
ACKNOWLEDGEMENTS.....	III
CONTENTS.....	IV
LIST OF TABLES.....	VI
LIST OF FIGURES.....	VII
CHAPTER	
I INTRODUCTION.....	1
1.1 Background.....	1
1.2 Significance of Study.....	4
1.3 Research objectives.....	6
1.4 Scope.....	6
II THEORY.....	7
2.1 Principle of Spectral Domain Optical Coherence Tomography (SD- OCT).....	8
2.2 Film thickness and topography.....	12
III METHODS.....	16
3.1 Biofilm cultivation.....	16

CONTENTS (Continued)

	Page
3.2 Experimental setup of the OCT topographic microscope.....	17
3.3 OCT Topography Procedure.....	23
3.4 Sub-region thickness analysis.....	27
IV RESULTS AND DISCUSSIONS.....	29
V CONCLUSION.....	36
REFERENCES.....	37
CURRICULUM VITAE.....	43



LIST OF TABLES

Table	Page
3.1	Comparison of the measurement result of total thickness from digital micro-meter and optical topography technique of a glass plate.....27



LIST OF FIGURES

Figure		Page
2.1	A typical layout of spectrometer-based SD-OCT	6
2.2	Schematic shows the sample reflectivity along depth and the resolved depth profile that is the convolution between an axial point spread function and the Sample reflectivity	12
2.3	Schematic shows the top and bottom surface of a glass plate reflectivity Along depth.....	13
2.4	Schematic shows creating the resolved depth profile by the convolution between an axial point spread function and the top and bottom surface of a glass plate reflectivity.....	14
3.1	An illustration of biofilm cultivation.....	17
3.2	(a) Diagram of the OCT topographic microscope. (b) A photograph of the setup.....	18
3.3	(a) Diagram of the designed high-speed infrared spectrometer. (b) A photograph of the setup.....	19

LIST OF FIGURES (Continued)

Figure	Page
3.4	(a-c) Some examples of spectral interference signals as detected by the spectrometer and (d-f) its corresponding depth profiles obtained through the Fourier analysis. (g) The relation between the position of amplitude in pixel and the translation distance of the reference mirror measured in micrometer. (h) The zoom in of the axial PSF in calibrated scale for measuring of the axial resolution of the system..... 21
3.5	Plot of the peak amplitude of the FD-OCT signals measured at different depth positions in air..... 22
3.6	(a) is picture of resolution target from SD-OCT and (b) is Table resolution values for standard (USAF1951) 23
3.7	An illustration of processing details for acquired surface and optical thickness topography from 3D OCT dataset..... 24
3.8	(a) interference data of a glass plate. (b) depth profile. (c) xy-map of the 1 st peaks' location (top surface). (d) xy-map of the 2 nd peaks' location (bottom surface)..... 25
3.9	(a) xy-map OCT Thickness Topography of a glass plate. (b) top view OCT Thickness Topography in (a)..... 26
3.10	Digital micrometer for measuring thickness of a glass plate..... 26

LIST OF FIGURES (Continued)

Figure	Page
3.11	An illustration of sub-region thickness analysis. (a) OCT thickness topography obtain in section 3.3. (b) Example of 5×5 sub-region thickness analysis method by computing mean and SD in each sub-region. (c) A map of the mean thickness of each sub-region, showing the thickness distribution of the thin film. (d) A map of the SD of the thickness in each sub-region, showing the thickness uniformity of the thin film..... 28
4.1	(a-e) Top view of OCT image developed on copper material (a. pre-colonization, b. day 7 c. day 14, d. day 21, e. day 28) bar scale is 1 mm and SEM on day 28 (f) bar scale is 10 μm, magnification 1300× and (g-j) is cross-sectional images of biofilm on copper surface in 4 weeks..... 30
4.2	Biofilm in the 3 rd week; (a) Top surface xy-map of peaks location and (b) Bottom surface xy-map of peaks location; (c) 3D surface plot of optical thickness topography of biofilm; (d) 2D map of the optical thickness topography of the biofilm..... 31
4.3	Biofilm in 4 th weeks, Top surface xy-map of peaks location show in (a) and bottom surface xy-map of peaks location show in (b). Optical thickness topography of biofilm shows in (c) and (d) is top view of optical thickness topography..... 32

LIST OF FIGURES (Continued)

Figure		Page
4.4	Sub-region optical thickness and its SD overlay on top of with en face OCT image of the biofilm during (a) 3 weeks and (b) 4 weeks of culture, respectively. A color map of the optical thickness of biofilm in week 3 and week 4 are shown in (c) and (d), respectively, (e) and (f) is a color map of the SD of the optical thickness of the biofilm in week3 and week4, respectively.....	34
4.5	3D surface profiles of the sub-region thickness topography of the biofilm development in week 3 and week 4 are shown in (a) and (b), respectively.....	35

CHAPTER I

INTRODUCTION

1.1 Background

Biofilm formation have been found to contribute to a variety of problems on plants, water, environment and human health. Study of biofilm to analyze its structure to prevent its formation and impacts on surface of materials is thus crucial.

Studies of biofilm formation on surfaces are quite extensive. Most commonly used techniques for investigating biofilm characteristics are, for example, bright field microscopy, fluorescence microscopy, Fourier transform infrared (FTIR) spectroscopy, and scanning electron micrograph (SEM). Focusing on biofilm composition, these techniques are quite destructive and require complicate sample preparation. In all cases, the biofilm sample need to be dried, which makes the study of biofilm in its original form not possible. The improvement of more rapid and sensitive techniques for the detection and quantification of living cells would contribute to a more understanding of biofilm formation, particularly when they are monitored in actual environment.

Thickness of thin film is one of the most significant parameters for film characterization. There are also many techniques for measuring thickness of thin film, such as SEM and ellipsometry. However, it is difficult for these techniques to measure film thickness of biofilm in its actual environment. Optical coherence tomography (OCT) is an emerging optical imaging technology that can provide depth cross sectional image of biological sample at micrometer level resolution (Huang et al.,1991)

OCT is capable of high speed imaging, which allows for 3D measurement of multi-stacked thin films (Meemon et al., 2014). OCT topography can measure thickness, shape, and features of thin film by using the principle of interference of backscattered light from its top and bottom surfaces. Several techniques of OCT tomography for measurement of thickness and surface of samples, e.g. thin films on copper surface (Debnath et al., 2006; S.W. Kim and Kim, 1999; Qin et al., 2013), polymeric materials (Meemon et al., 2013; Yao et al., 2013), and biological tissues (Hee et al., 1998; Sun et al., 2014), have been investigated and reported.

Thin film materials, whose thickness is at micrometer or nanometer scale have been used in research and industry (Baer et al., 2006). One important feature of thin films is thickness uniformity. Topography technique is another interesting technique for imaging of the thickness and the surface of thin films. For example, a silicon (Si) wafer is very important as a substrate of semiconductor products such as integrated circuit (IC) chips, light emitting diodes (LEDs), solar cells, and MEMS devices. The use of OCT tomography and topography to measure uniformity of the surface and uniformity of thickness of Si wafer has been verified (Y. G. Kim et al., 2013). In addition, the technique has also been used to inspect Liquid Crystal Display (LCD) to find the causes of defects. It can address the problems involving the process of fabrication, protect losses due to production line stoppages, and satisfy users regarding LCD reliability (S.H. Kim et al., 2011). OCT has also been used in measurement of thickness of thin film and investigate coating quality. Coating quality is one of the most significant parameters for film characteristics (Qin et al., 2013). In addition, it was used to quantify 3D film thickness and homogeneity of multi-stacked polymeric films (Meemon et al., 2013).

Over the past several years, the study of surface associated with biofilm has been widely investigated. Biofilm creation is caused by the growth of microorganisms, with extracellular polymeric substances (EPS) produced by them, on a material surface. It causes various problems such as bacterial contamination, biofouling, biocorrosion in manufacturing and household water systems, and persistent microbial infections in human (Damodaran et al., 2016; Fortunato et al., 2017; Horie et al., 2016). A crucial perspective of the biofilm studies is the analysis of biofilm structure (Xu et al., 2015), which can predict the biofilm formation and its impact on the surface of material.

Various microscopic techniques such as scanning electron microscopy (SEM) and confocal laser scanning microscopy (CLSM) are considered as important tools for biofilm structure investigation. Nonetheless, as mentioned earlier, these techniques normally require complicated sample preparation, and are less suitable for monitoring the development of biofilm *in situ*. The techniques are generally performed *ex situ* and destroy samples when each experiment is completed. Therefore, they are not capable for monitoring the structural formation of biofilm. To fully understand the biofilm progress on surface, *in situ* qualitative and quantitative analysis of the biofilm under various conditions are demanded.

Recently, OCT has been used for the study of biofilm formation under decontaminated operational conditions. It is capable of simultaneous quantification of biofilm structure and the related flow velocities, and biofilm growth in a microfluidic channel (Weiss et al., 2016). In addition, OCT allows online monitoring of biofilm growth and detachment in a flow channel and monitoring of biofilm density using acquired 2D and 3D image. OCT topographic image has also been used to monitor the

growth of biofilm and can be used for improvement of antifouling strategies and for process optimisation in wastewater treatment plants (Haisch and Niessner, 2007).

In recent years, several procedures to study thin film formation and destruction *in situ* by OCT have been reported in literature. There are several advantages of using OCT for studying thin film. First, OCT uses near infrared light that is completely non-invasive to biological sample. Second, OCT is a non-contact imaging technique and therefore no need for sample preparation. Third, the non-contact capability also allows for imaging the sample through a transparent cover of the sample's chamber to avoid contamination.

Recently, Weiss et al. (2016) investigated biofouling characteristics in dynamic culture, such as biofouling in microfluidic flow channel, using OCT. The flow velocity of biofouling, which varied with the growth of the biofouling in a microfluidic flow channel was measured. A clear change of the flow velocity was seen after more growth of biofouling (Weiss et al., 2016). OCT topographic image can be used for improvement of antifouling strategies and for process optimization in wastewater treatment plants which can be treated in a timely manner (Haisch and Niessner, 2007).

1.2 Significance of Study

Since 1976, a serious epidemic of *Legionella pneumophila* was first broken out in Philadelphia. *L. pneumophila* are non-spore forming gram-negative obligate aerobic bacteria living generally around in both natural and man-made aquatic environmental reservoirs for instant mud springs, water cooling towers and purification systems, shower heads and swimming pools (Collins et al., 2017; Costa et al., 2010; Hsu et al., 2009). Legionella diseases are frequently connected with direct bacterial interaction in

man-made aquatic environments, where appropriate water temperature (25-42 °C) and persistent biofilms support growth and survival of *L.pneumophila*. (Fields et al., 2002; Napoli et al., 2009; Steinert et al., 2002). Legionella is the significant waterborne bacteria because people can expose to the bacteria in aerosolized water droplets from contaminated water systems (Fields et al., 2002). Most analytical methods were developed but no currently unfilled test is able to diagnose all *L. pneumophila* include real-time *in vivo* monitoring of the *L. pneumophila*. (P. Edelstein et al., 1985; Roig et al., 1991).

The improvement of more rapid and sensitive techniques for the quantitative monitoring of *L. pneumophila* viable cells is important for monitoring water quality and legionellosis inhibition (Ditommaso, Ricciardi, Giacomuzzi, Arauco Rivera and Zotti, 2015). It is expected that OCT topographic imaging can be used to monitor the formation of *L. pneumophila* in its actual environment. Previous reports mostly focused on monitoring the growth of biofilm in water flow system by using OCT to measure the change in flow speed. However, the bacterial biofilm of *L. pneumophila* formation in still water (water tank, swimming pool) is much slower process than that of biofouling formation. The use of OCT for quantitative monitoring of biofilm formation over time never been reported and need to be established for such study.

As such, this study aims to evaluate the use of OCT topography techniques for quantitative monitoring of biofilm formation by study growth of the *L. pneumophila* biofilm in still water, which represents the growth of biofilm in water tank. A procedure to obtain optical thickness topography of biofilm and to quantify the thickness distribution and thickness uniformity of the biofilm formation for observing the growth of biofilm over certain period of its development has been developed. The proposed

technique allows for *in vivo* study of biofilm formation, which could be a useful tool for biologists to understand biofilm formation in various conditions and how to prevent them.

1.3 Research objectives

- 1) To develop an optical tomography technique for the characterization of thickness uniformity of biofilm sample
- 2) To use the developed procedure for online monitoring of *L. pneumophila* biofilm growth in still water over time periods

1.4 Scope

- 1) Design and built a topographic microscope based on the principle of SD-OCT.
- 2) Design and built data acquisition and signal processing to obtain optical thickness topography of thin film.
- 3) Develop Labview programming for data acquisition and signal processing.
- 4) Verify the developed system by measuring the thickness topography of a thin glass plate of known thickness.
- 5) Apply the developed system to monitor the development of *L. pneumopila* biofilm over 4 weeks period.
- 6) Develop sub-region topography to quantify the thickness distribution and to visualize the thickness uniformity of the biofilm.

CHAPTER II

THEORY

Optical techniques are usually the preferred method for measuring thin film since they are precise, non-invasive, non-destructive, and require little or no sample preparation. For example, ellipsometry is an optical system to measure the transmission and reflection properties after the light is incident on the sample. It can non-invasively measure sample, but it has low spatial resolution and data analysis becomes complicated (Rothen, 1945). Scanning electron microscope can measure thickness of sample with high resolution, but this technique normally requires complicated sample preparation and normally requires destruction of the sample (Cao et al., 2018).

OCT can produce high-resolution cross-sectional images of microstructures of living tissues and biological samples (Huang et al., 1991). Later, the technique has been introduced into biofilm research (Xi et al., 2006). One of the most attractive features of OCT is that it uses safe near infrared light instead of hazardous ionizing radiation.

There are two primary types of OCT implementations called time-domain OCT (TD-OCT) and spectral-domain OCT (SD-OCT) (Fercher et al., 1995; Huang et al., 1991). TD-OCT measure the temporal interference of a broadband light beam and hence requires mechanical scanning of its reference mirror to obtain depth sectioning image, which greatly limits its imaging speed (Huang et al., 1991). In contrast, SD-OCT measures light interference in spectral domain without the need for scanning of the reference mirror as shown in Figure 2.1, which greatly improves the imaging speed (Fercher et al., 2003).

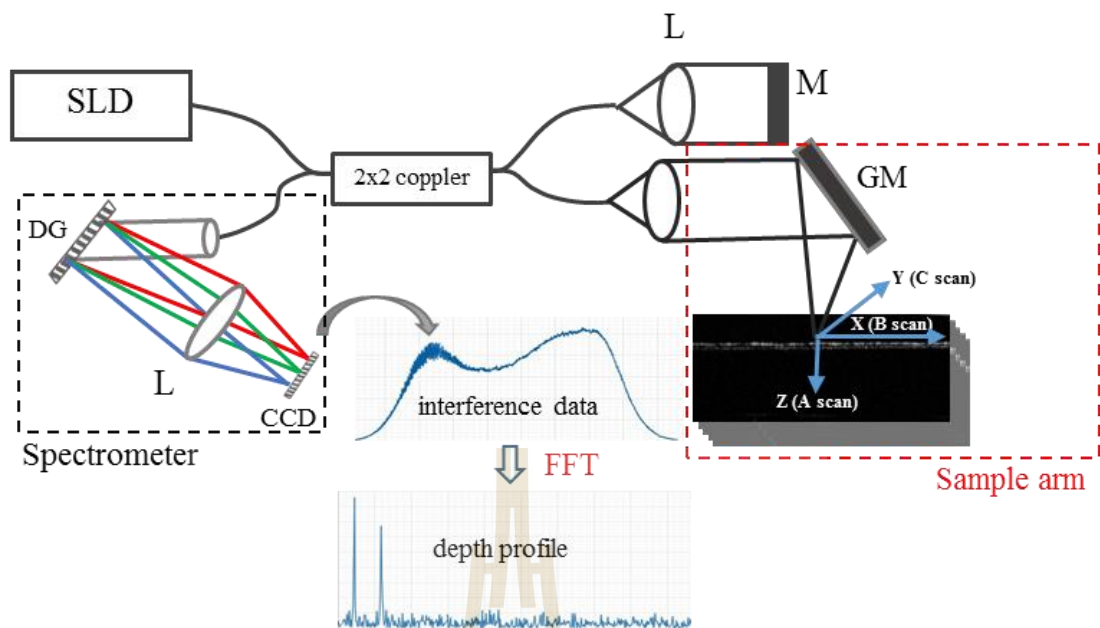


Figure 2.1 A typical layout of spectrometer-based SD-OCT; SLD = superluminescent diode, L = lens, M = mirror, GM = Galvanometer mirror, DG = diffraction grating, CCD = charge-coupled device, FFT = fast Fourier transform.

2.1 Principle of spectral domain optical coherence tomography (SD-OCT)

From figure 2.1 the light beam from the SLD light source is coupled to a single mode fiber and split into two beam paths by a fiber coupler with 50:50 power split ratio. 50% of the power goes to the reference arm and another 50% goes to the sample arm. Light reflected from the reference mirror is coupled back to the fiber and delivered back to the fiber coupler. The sample beam path consists of a fiber coupler, a galvanometer scanning mirror, an objective lens, and sample holder stage. Light from sample collimator is incident on the galvanometer mirror, redirected to the objective lens, and focused on the sample. Backscattered light from within the sample is collected by the

same objective and delivered back to the fiber coupler. The reference and sample light beams are then interfered and recorded by a spectrometer. Fourier transformation of the captured spectral interference data yields depth profiles. The spectral intensity detected by the spectrometer can be expressed as

$$\hat{I}_D(k) = |\hat{E}_R(k) + \hat{E}_S(k)|^2, \quad (2.1)$$

$$\hat{I}_D(k) = (\hat{E}_R(k) + \hat{E}_S(k))(\hat{E}_R^*(k) + \hat{E}_S^*(k)), \quad (2.2)$$

$$\hat{I}_D(k) = \hat{E}_R(k)\hat{E}_R^*(k) + \hat{E}_R(k)\hat{E}_S^*(k) + \hat{E}_S(k)\hat{E}_R^*(k) + \hat{E}_S(k)\hat{E}_S^*(k), \quad (2.3)$$

$$\hat{I}_D(k) = |\hat{E}_R(k)|^2 + |\hat{E}_S(k)|^2 + 2Re\{\hat{E}_R(k)\hat{E}_S^*(k)\}, \quad (2.4)$$

where the caret denotes a function in the spectral domain, $\hat{E}_R(k)$ is the spectral electric field after round-trip propagating along the reference beam path, and $\hat{E}_S(k)$ is the spectral electric after round-trip propagation along the sample path.

The spectral electric field traveling from reference arm, $\hat{E}_R(k)$, can be defined as

$$\hat{E}_R(k) = K_R \hat{E}_{R0}(k) r_R \exp(jkl_R), \quad (2.5)$$

where $k = \frac{2\pi}{\lambda}$ is the wave propagation number, K_R is a real number of total losses in the reference arm, $\hat{E}_{R0}(k)$ is the spectral electric field amplitude in the reference arm right after the beam splitter, r_R is the reflectivity of the reference mirror and l_R is a round-trip propagation distance along the reference arm. The spectral electric field traveling from the sample, $\hat{E}_S(k)$, is a collection of many backscattering events happening at various depths that can be modeled as

$$\hat{E}_S(k) = K_S \hat{E}_{S0}(k) \int_{-\infty}^{+\infty} r_S(l_S) \exp(jkl_S) dl_S, \quad (2.6)$$

where K_S is a real number representing total losses in the sample path, $\hat{E}_{S0}(k)$ is the spectral electric field amplitude in the sample arm right after the beam splitter, l_S is a round-trip optical path length along the sample arm, and $r_S(l_S)$ represents the sample reflectivity profile along the depth as a function of l_S (Wang and Wu 2007). By assuming that the beam splitter is perfect, $\hat{E}_{R0}(k) = \hat{E}_{R0}(k) = \hat{E}_0(k)$, the spectral intensity in Eq. (2.4) can be rewritten as

$$\hat{I}_D(k) = |\hat{E}_0(k)|^2 \cdot \left[|K_R r_R|^2 + 2K_R K_S r_R \int_{-\infty}^{+\infty} r_S(l_S) \cos(k(l_S - l_R)) dl_S + \left| K_S \int_{-\infty}^{+\infty} r_S(l_S) e^{jkl_S} dl_S \right|^2 \right], \quad (2.7)$$

The first term is regarded as DC-term that can be measured by blocking the signal from the sample arm and hence can be removed through the direct subtraction method. The third term is the auto-correlation term (AC-term) that is a collection of interference of backscattering signals from different depths in the sample arm. It is much smaller than the first term and the second term (i.e. $r_S \ll r_R$) so that it can be neglected. A strong autocorrelation from the sample arm can be removed by blocking the reference arm then taking the subtraction. The second term is interference between sample and reference beams by setting the optical path length difference $l_D = l_S - l_R$ and assuming that the DC and auto-correlation terms (first term and third term) can be removed, the spectral interference signal can be expressed as

$$\hat{I}_{int}(k) = 2K_R K_S r_R \hat{S}(k) \cdot \int_{-\infty}^{+\infty} r_S(l_D) \cos(k(l_D)) dl_D, \quad (2.8)$$

where $\hat{S}(k) = |\hat{E}_0(k)|^2$ represents the power spectral density of the light source and $r_S(l_D)$ is the sample reflectivity profile as a function of the optical path length difference l_D . Using the identity $\cos(x) = \frac{1}{2}(e^{+ix} + e^{-ix})$, Eq. (2.8) can be expressed

$$\hat{I}_{int}(k) = K_R K_S r_R \hat{S}(k) \cdot \left[\int_{-\infty}^{+\infty} r_S(l_D) \exp(ikl_D) dl_D + \int_{-\infty}^{+\infty} r_S(l_D) \exp(-ikl_D) dl_D \right], \quad (2.9)$$

In addition, from the definition of Fourier transform as

$$\mathfrak{F}\{f(x)\} = \int_{-\infty}^{+\infty} f(x) \exp(jkx) dx \quad (2.10)$$

and using the property $f(-x) \Leftrightarrow F(-k)$ (Beyer, 1991), Eq. (2.10) can be rewritten as

$$\hat{I}_{int}(k) = K_R K_S r_R \hat{S}(k) \cdot [\mathfrak{F}\{r_S(l_D)\} + \mathfrak{F}\{r_S(-l_D)\}], \quad (2.11)$$

Consequently, the inverse Fourier transform of Eq. (2.11) is given by

$$I_{OCT}(l_D) = K_R K_S r_R \mathfrak{F}^{-1}\{\hat{S}(k)\} * [r_S(l_D) + r_S(-l_D)], \quad (2.12)$$

Eq. (2.12) shows that the sample reflectivity profile along depth can be achieved by the inverse Fourier transform of the measured spectral interference signal. The $\mathfrak{F}^{-1}\{\hat{S}(k)\}$ represents the axial point spread function (PSF). The resolved depth profile is a convolution between the axial PSF and the symmetry function of the sample reflectivity that is $r_S(-l_D)$ and $r_S(l_D)$ as shown in Figure 2.2.

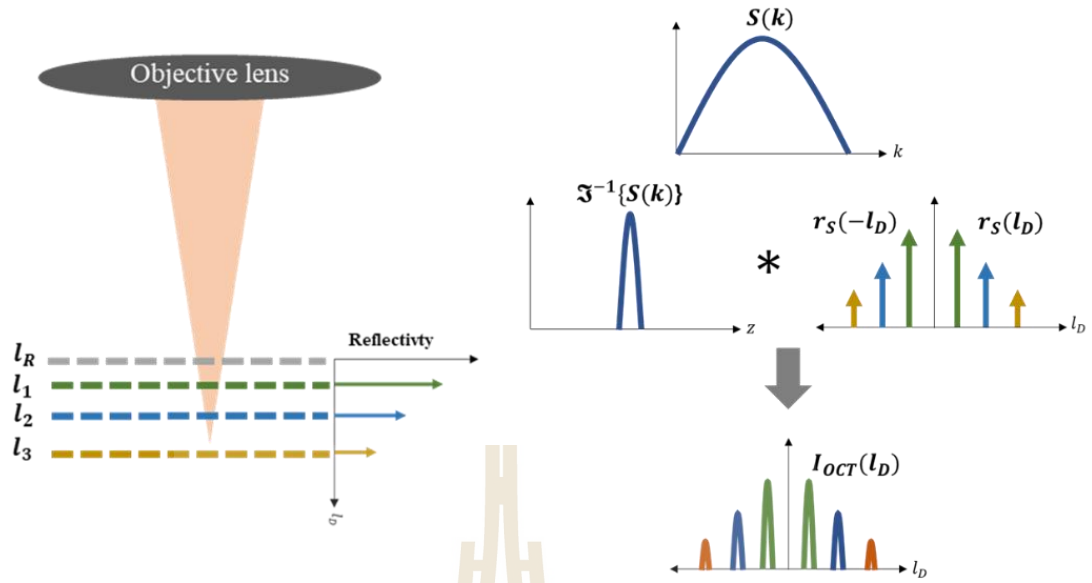


Figure 2.2 Schematic shows the sample reflectivity along depth and the resolved depth profile that is a convolution between an axial point spread function and the sample reflectivity.

2.2 Film thickness and topography

Considering a glass plate as a sample as shown in Figure 2.3, Eq. (2.6) becomes

$$\hat{E}_S(k) = K_S \hat{E}_0(k) [r_{S1}(\exp(jkl_{S1}) + r'_{S2} \exp(jkl_{S2}))], \quad (2.13)$$

where r'_{S2} is $r_{S2}(1 - r_{S1})$, l_{S1} and l_{S2} are a round-trip optical path length along the sample arm at the top and bottom surface of glass plate, and r_{S1} and r_{S2} represents the sample reflectivity at the depth l_{S1} and l_{S2} , respectively.

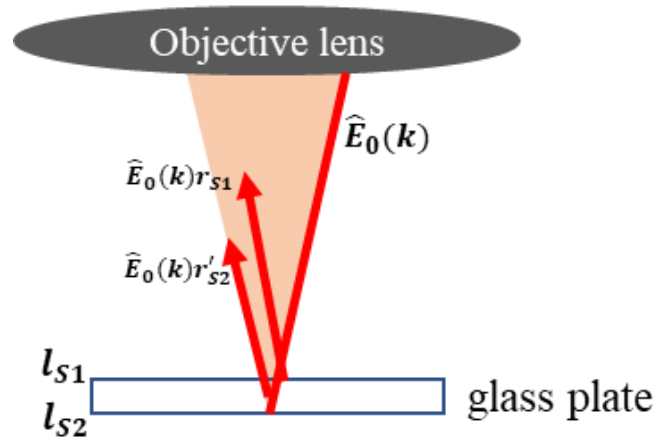


Figure 2.3 Schematic shows the top and bottom surface of a glass plate reflectivity along depth.

Therefore, from Eq. (2.3), we get

$$\begin{aligned}
 \hat{I}_D(k) = & |\hat{E}_0(k)|^2 \cdot \left(|K_R r_R|^2 + |K_S r_{S1}|^2 + |K_S r'_{S2}|^2 + \right. \\
 & K_S r_{S1} K_R r_R |E_0(k)|^2 e^{jkl_{S1} - jkl_R} + K_S K_R r_R r'_{S2} |E_0(k)|^2 e^{jkl_{S2} - jkl_R} + \\
 & K_S r_{S1} K_R r_R |E_0(k)|^2 e^{jkl_R - jkl_{S1}} + K_S K_R r_R r'_{S2} |E_0(k)|^2 e^{jkl_R - jkl_{S2}} + \\
 & \left. r_{S1} r'_{S2} |K_S E_0(k)|^2 e^{jkl_{S2} - jkl_{S1}} + r_{S1} r'_{S2} |K_S E_0(k)|^2 e^{jkl_{S1} - jkl_{S2}} \right). \quad (2.14)
 \end{aligned}$$

The first to the third term is regarded as DC-term. The eighth and ninth term are the auto-correlation term (AC-term) that is negligible. The fourth to the seventh term are interference between sample and reference arm. We will assume that the DC and auto-correlation terms can be removed and there is no loss in both paths. By setting the optical path length difference $l_{D1} = l_{S1} - l_R$ and $l_{D2} = l_{S2} - l_R$ the spectral interference signal can be expressed as

$$\hat{I}_D(k) = K_S K_R r_R \hat{S}(k) \cdot \left(r_{S1} e^{jkl_{D1}} + r'_{S2} e^{jkl_{D2}} + r_{S1} e^{-jkl_{D1}} + r'_{S2} e^{-jkl_{D2}} \right), \quad (2.15)$$

$$\hat{I}_D(k) = K_S K_R r_R \hat{S}(k) [r_{S1} \cos(kl_{D1}) + r'_{S2} \cos(kl_{D2})], \quad (2.16)$$

The reflectivity profile of top and bottom surface of a glass plate along depth can be obtained by the inverse Fourier transform of Eq. (2.16), which yields

$$I_{OCT}(l_D) = K_S K_R r_R \mathfrak{F}^{-1}(\{\hat{S}(k)\}) * [r_{S1}\delta(l_D - l_{D1}) + r_2'\delta(l_D - l_{D2}) + r_{S1}\delta(l_D + l_{D1}) + r_2'\delta(l_D + l_{D2})]. \quad (2.17)$$

Eq. (2.17) reveals that OCT depth profile is a convolution between an axial point spread function, $\mathfrak{F}^{-1}\{\hat{S}(k)\}$, and an even symmetric function of the sample reflectivity that are $r_{S1}\delta(l_D - l_{D1})$, $r_2'\delta(l_D - l_{D2})$, $r_{S1}\delta(l_D + l_{D1})$ and $r_2'\delta(l_D + l_{D2})$ as shown in Figure 2.4. Therefore, the location of the maxima of $I_{OCT}(l_D)$ represents the location of the reflectors.

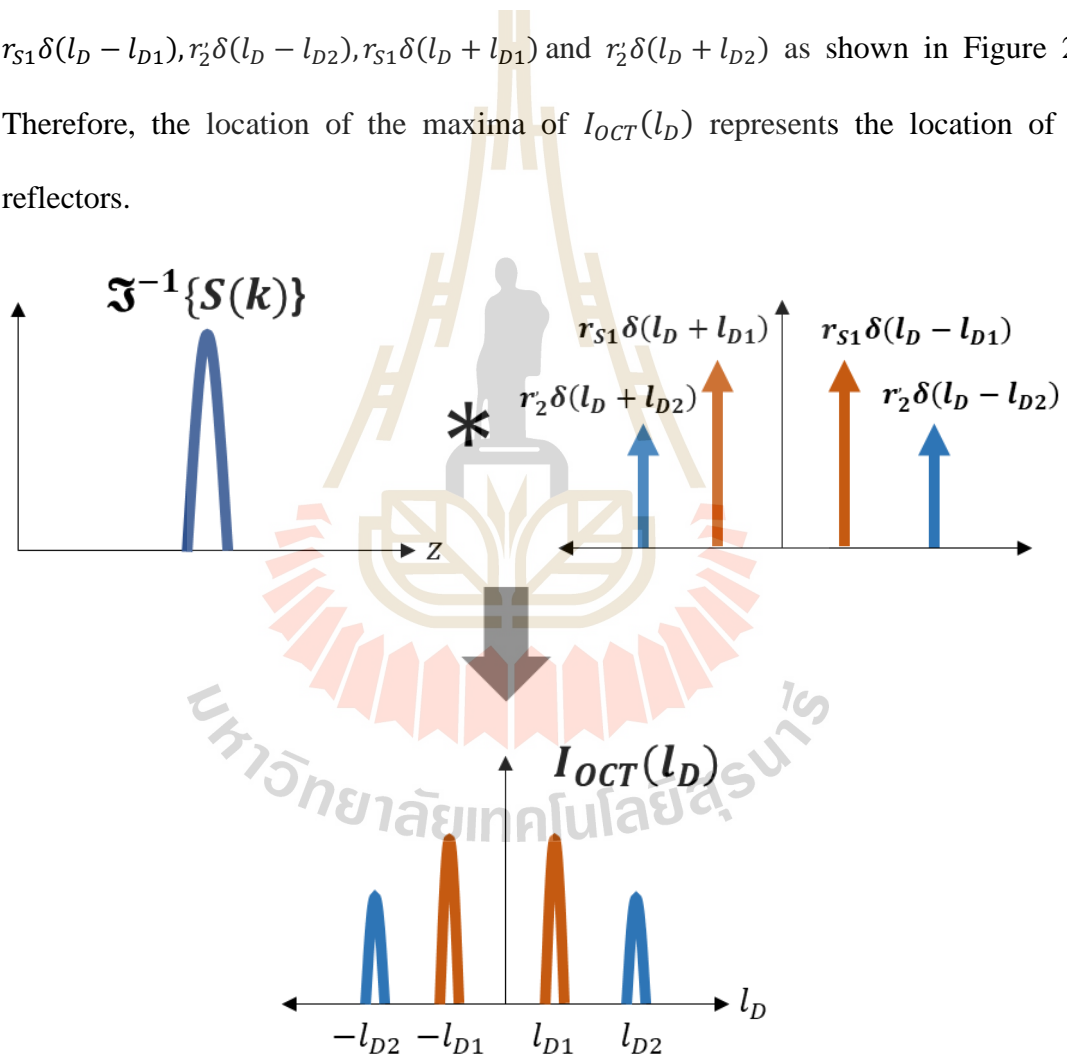


Figure 2.4 Schematic shows creating the resolved depth profile by the convolution between an axial point spread function and the top and bottom surface of a glass plate reflectivity.

Combining with lateral scanning, i.e. XY plane, we obtain

$$I_{OCT}(x, y, l_D) = K_S K_R r_R \mathfrak{F}^{-1}(\{\hat{S}(k)\} * [r_{S1}(x, y)\delta(l_D - l_{D1}(x, y)) + r'_2(x, y)\delta(l_D - l_{D2}(x, y)) + r_{S1}(x, y)\delta(l_D) + r'_2(x, y)\delta(l_D)]), \quad (2.18)$$

Tracking the location of maxima of each axial PSF across the XY-plane yields topography of reflection surface, i.e. $l_{D1}(x, y)$ and $l_{D2}(x, y)$ for topography of the top and bottom surfaces, respectively.



CHAPTER III

METHODS

3.1 Biofilm cultivation

The *Legionella pneumophila* biofilm was grown on surface of a copper plate. To allow *in-situ* non-destructive observation of the biofilm formation by OCT, the copper plates were contained in 12 cell well plate with cover. During the four weeks experimental period, the *Legionella pneumophila* biofilm development was monitored by OCT imaging.

The bacterial cells examined during this study were inoculated in sterile buffered yeast extract (BYE) broth, based on Edelstein's formula with minor modification, which contains N-(2-acetoamino)-2-amino-ethanesulphonic acid (ACES) 5 g/l; yeast extract 10 g/l; supplemented with L-cysteine 0.4 g/l and ferric pyrophosphate 0.25 g/l then adjusts to pH 6.9 with 1N KOH (P. H. Edelstein, 1981). The bacteria was grown at 37 °C for 3 days for experiment. The copper plate (10x10 mm) was be used for the biofilm formation. The copper plates were sterilized by autoclave (121 °C 15 minute). The biofilms was grown on sterile copper plate by inoculated with 3 milliliter (ml) *L. pneumophila* medium in 12 well cell culture plates as shown in Figure 3.1. The bacteria medium was changed every 7 days.

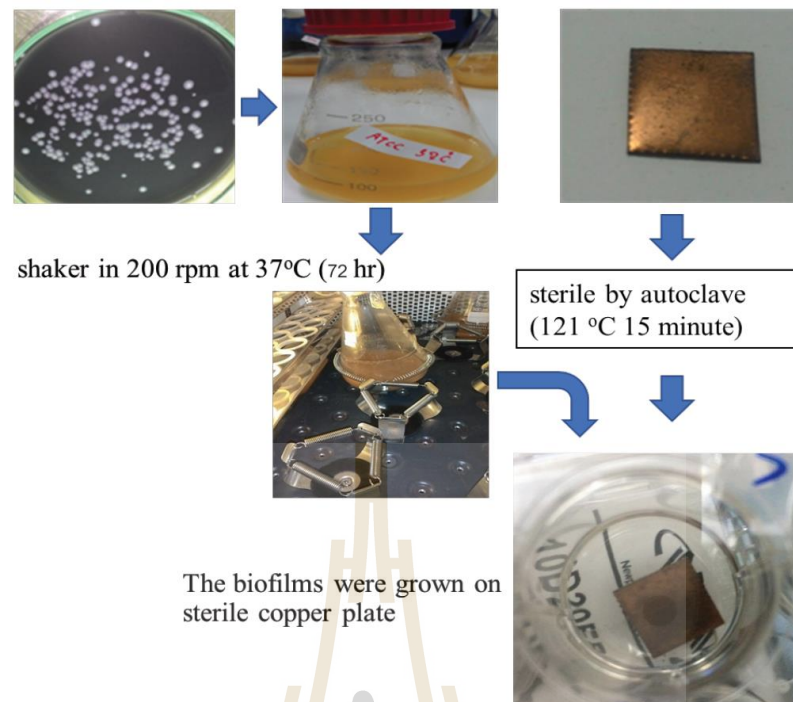


Figure 3.1 An illustration of biofilm cultivation.

3.2 Experimental setup of the OCT topographic microscope

An optical thickness topographic microscope system based on SD-OCT principle was developed in this project, which was able to capture 2D and 3D image of thin film by using low-coherence light with a central wavelength (λ_0) of 880 nm and a full spectral range of about 120 nm (Near infrared, NIR). The developed system was based on the principle of low-coherence interferometry. The system measured spectral interference signal between light reflected from sample arm and reference arm (Meemon et al., 2014). The interference was detected by using a custom built spectrometer, so called a spectral interference signal (Born and Wolf, 1999). Fourier transform of the acquired spectral interference from spectrometer will yielded depth profile that was used to produce 2D and 3D image of thin film sample in about 10 second. The diagram of the experimental setup is shown in Figure 3.2

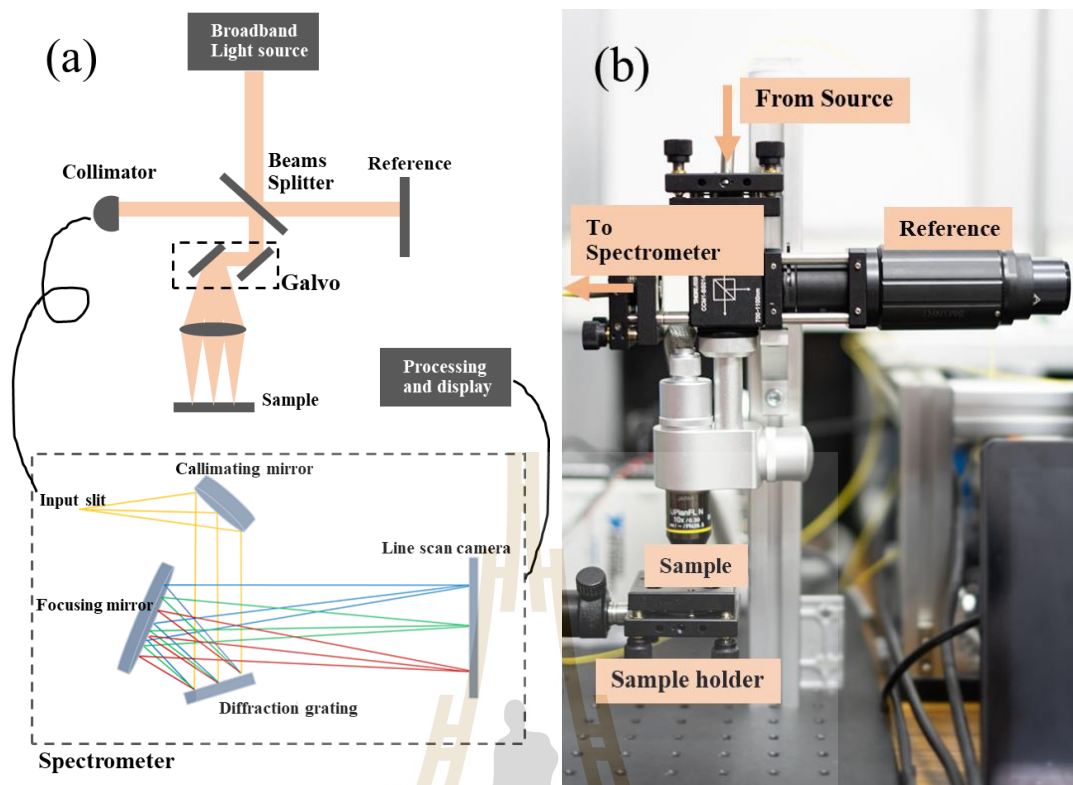


Figure 3.2 (a) Diagram of the OCT topographic microscope. (b) A photograph of the setup.

The detection and recording signal are the key to determine the speed of the topographic microscope system. The signal detection system consists of the main parts is an array photo-receiver. In this system, we use complementary metal-oxide-semiconductor (CMOS) (Mars2048-L51 gm, CONTRASTECH) with a small pixel size of $10\mu\text{m} \times 10\mu\text{m}$ a total number of pixels of 2048, and a line rate speed of 51kHz for the signal detection of the implemented spectrometer. The selection of CMOS type sensor has advantages in the speed of signal detection, which is appropriate for developing a high-speed spectrometer. Moreover, the optical system consists of a 90-degree off-axis parabolic mirror 83.3 mm focal length to collimate the input light beam from a single mode fiber optics, a reflective grating at 1200 lines/mm, and a 45-degree off-axis parabolic mirror to focus light beam on the sensor as shown in Figure 3.3.

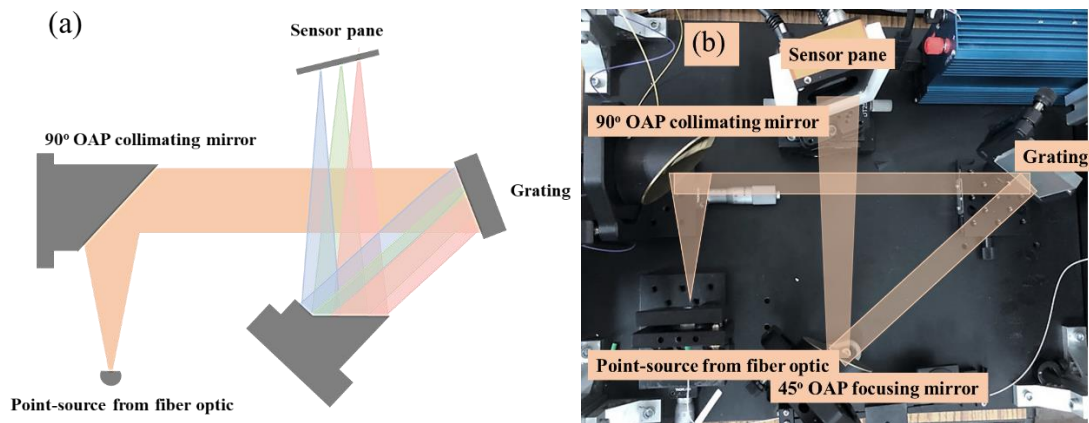


Figure 3.3 (a) Diagram of the designed high-speed infrared spectrometer. (b) A photograph of the setup.

In general, any spectrometer will possess two types of spectral resolution that are the digital resolution determined by the number of sensor pixel per line-scan and the optical resolution governed by the performance of the optical design and alignment of all optical components of the spectrometer. When using the spectrometer as a detector in SD- OCT system, an effective spectral resolution of the implemented spectrometer can be characterized through the measurement of the modulation depth of spectral fringes at different depth positions. In our measurement, we measured the axial PSFs at 27 different depth positions with 100 μm apart and extracted their peak amplitudes and positions. An example of a spectral interference fringe at arbitrary depth position is demonstrated in Figure 3.4(a-c). It is known that the finite spectral resolution will lead to reduction of the fringe visibility (i.e. the modulation amplitude) as the fringe frequency increases. This effect appeared as the amplitude dropping of an axial point spread function (PSF) over depth after the Fourier transformation of the spectral fringe as illustrated in Figure 3.4(d-f).

Figure 3.4(g) shows a plot between the peak location of the depth profile in pixels and the translation distance of the movable mirror in micrometer. The slope of the plot was used for calibration of the depth scale of the depth scan. In this system, we found that the size of one pixel equals to the actual depth distance in air of $5.07 \mu\text{m}$. Moreover, by using this depth scale to calibrate the depth profile signal, the axial resolution of the system can be determined from the FWHM of a single axial PSF as shown in Figure 3.4(h). The axial resolution was measured to be about $10 \mu\text{m}$.

Figure 3.5 show superposition of multiple depth profiles obtained at different positions of the sample. In this measurement, a perfect mirror was used as a sample. Therefore, there is only one reflection from the sample and hence only one peak in each capture depth profile. The drop trend of the amplitude of the signal over depth is caused

by the combination of finite spectral resolution of the spectrometer, dispersion mismatch between the sample and reference beam paths, and polarization mismatch between the sample and reference beam paths. This effect governs the maximum imaging depth of the measurement system, which is typically determined by the 10 dB fall-off of the amplitude, i.e. an amplitude drop of about 10 times as compared with the maximum amplitude. Therefore, the maximum imaging depth of this system was about 2.5 mm in air.

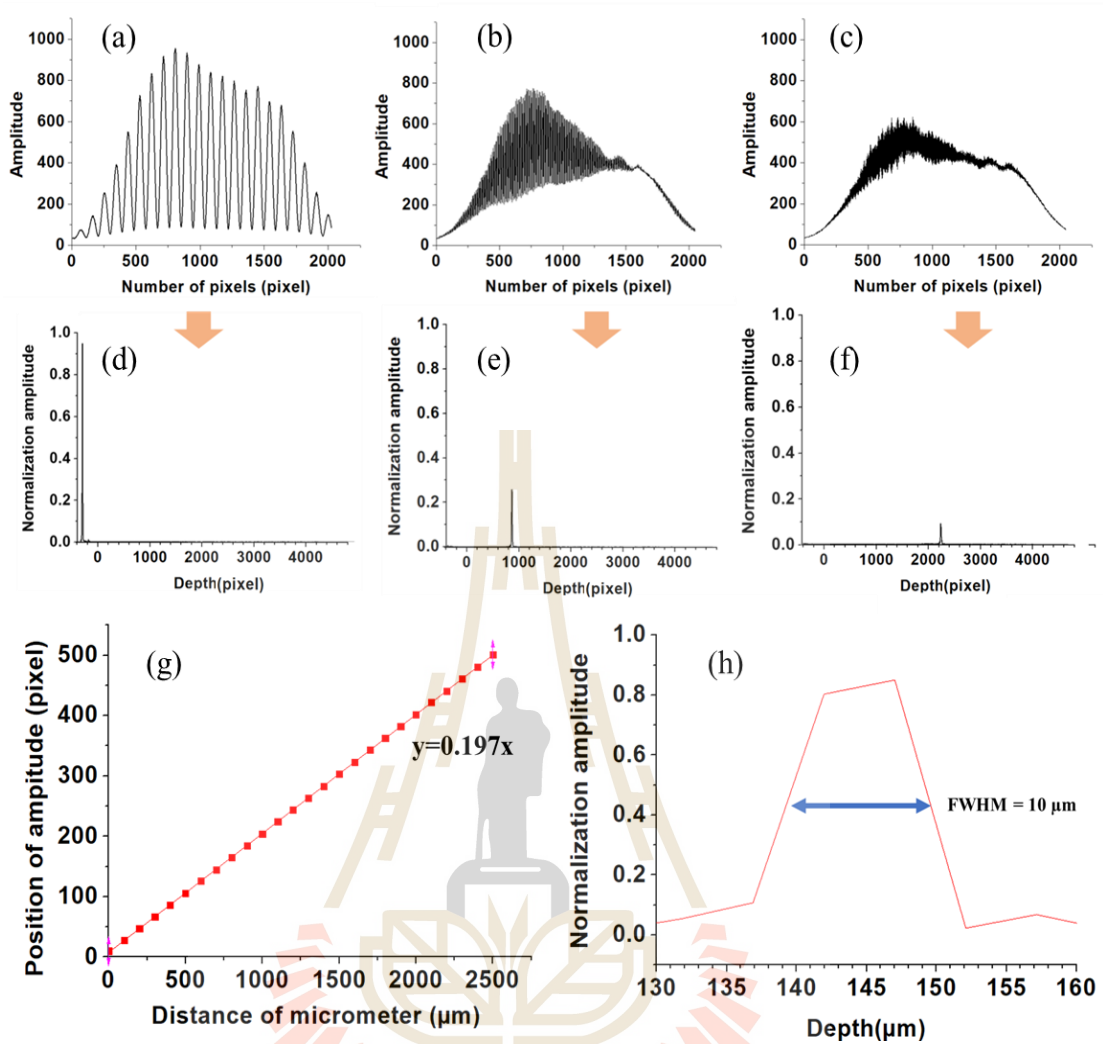


Figure 3.4 (a-c) Some examples of spectral interference signals as detected by the spectrometer and (d-f) its corresponding depth profiles obtained through the Fourier analysis. (g) The relation between the position of amplitude in pixel and the translation distance of the reference mirror measured in micrometer. (h) The zoom in of the axial PSF in calibrated scale for measuring of the axial resolution of the system.

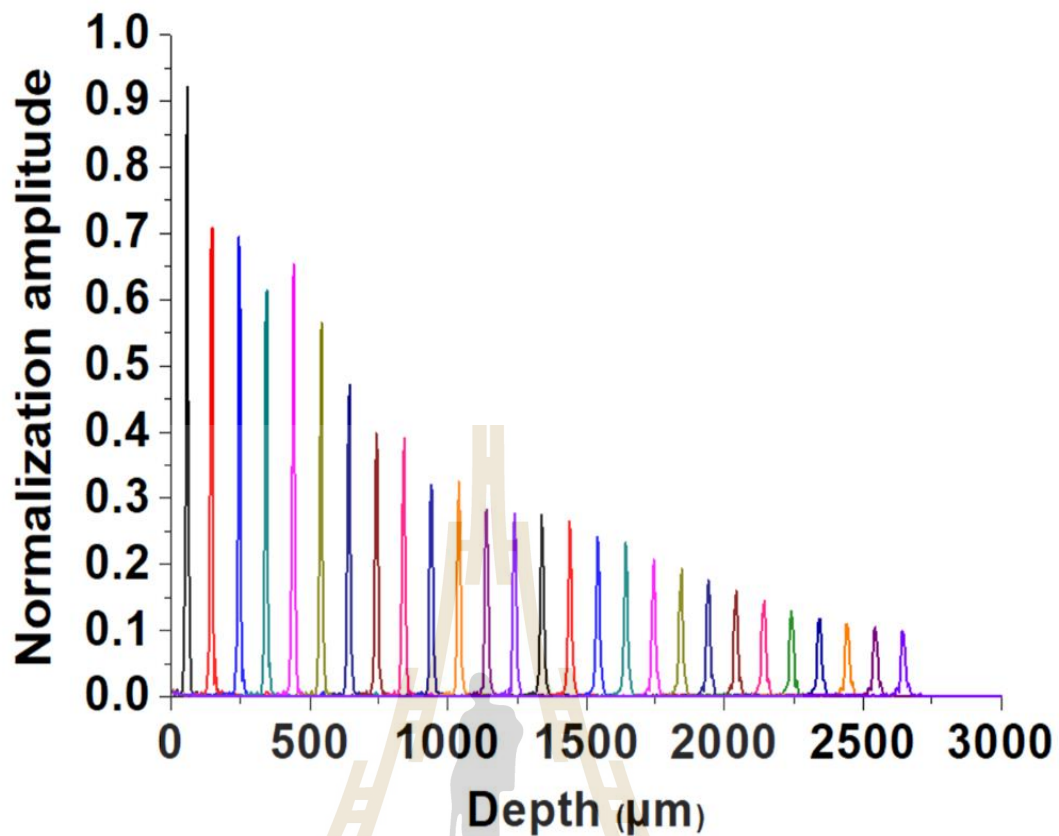


Figure 3.5 Plot of the peak amplitude of the FD-OCT signals measured at different depth positions in air.

In addition, the lateral resolution of the system was quantified by taking a 3D image of a USAF1951 resolution target as shown in Figure 3.6. The imaging result shows that the developed system can resolve the pattern down to at least the 1st element of group +7 of the resolution target as designated by red solid line circle in Figure 3.6(a). This corresponds with a spatial frequency of the pattern of 128 line pairs per millimeter, which can be convert to a lateral resolution of about 4 μm .

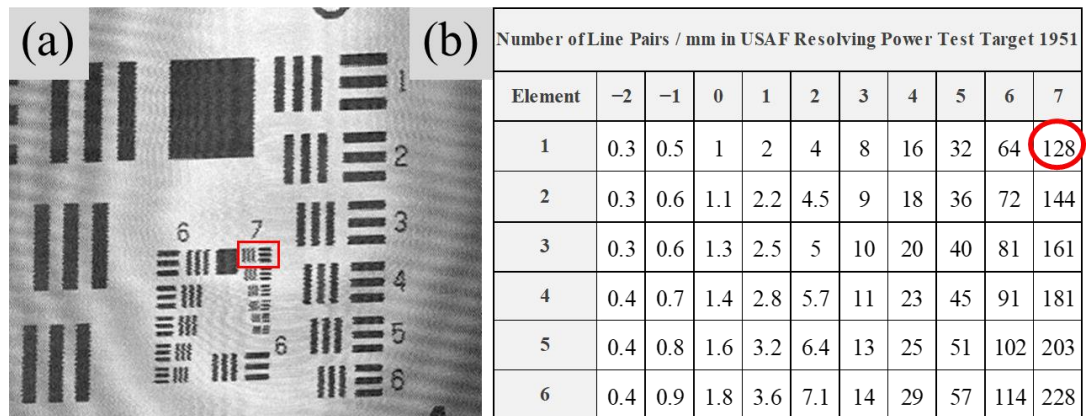


Figure 3.6 (a) is picture of resolution target from SD-OCT and (b) is Table resolution values for standard (USAF1951).

3.3 OCT topography procedure

Qualitatively, OCT imaging data (both 2D and 3D) provides a non-destructive approach to immediately look at sub-surface micro-structures of the biofilm. For quantitative measurement of the biofilm development, we developed an algorithm to extract optical thickness topography of the biofilm from its 3D OCT image. Figure 3.7 illustrates the flow diagram of the algorithm to extract optical thickness topography. We have verified the developed procedure by comparing optical topography technique with the digital micrometer by measuring thickness of a glass plate.

First, we obtained OCT signal interference data of a glass plate from OCT system as shown in Figure 3.8(a). Second, taking Fourier transform of the interference data of a glass plate yields depth profile as shown in Figure 3.8(b). From each depth profile of an OCT image, the maximum interference between the beams (corresponding to peaks in the fast Fourier transforms (FFTs) of the interference signal data) occurs when refractive index changes from one layer to the next.

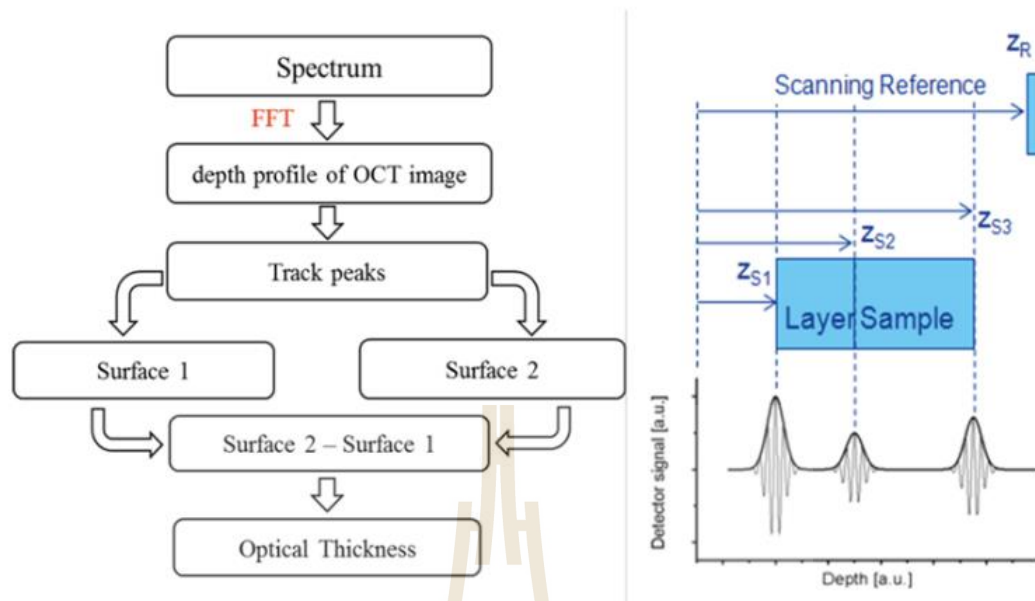


Figure 3.7 An illustration of processing details for acquired surface and optical thickness topography from 3D OCT dataset.

For the cross-sectional image of the glass plate, there are two clear distinguished interfaces that are the interface at the top and bottom surfaces of the glass plate. The maximum interference data between the beams occurs at every interface between two media of different refractive indices. Third, using a peak detection algorithm, the locations of top and bottom surfaces were obtained from each depth profile signal. By repeating the process for the whole 3D datasets, the topographic images of top and bottom interfaces were obtained. After tracking locations of peaks from each depth profile of 3D data, we obtain locations of peaks across the X-Y plane of the top and bottom surface of a glass plate as shown in Figure 3.8(c) and (d), respectively.

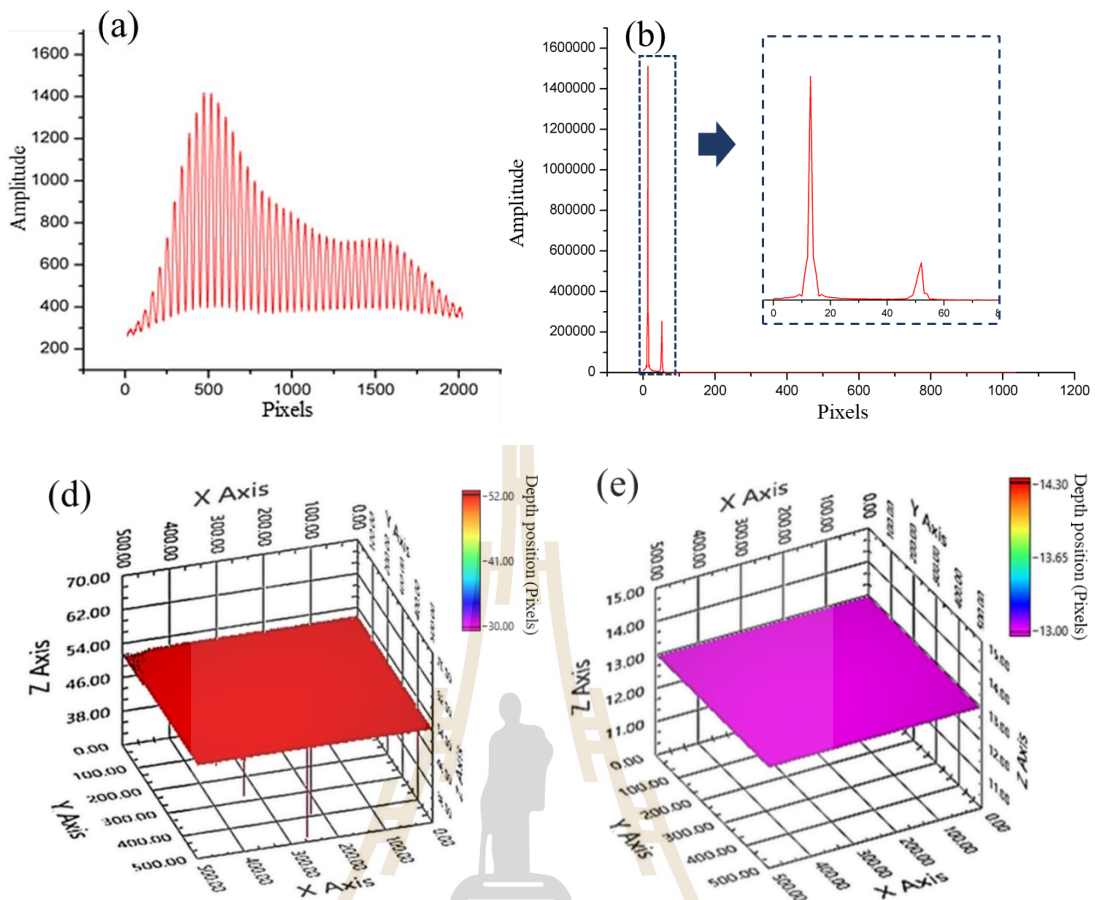


Figure 3.8 (a) interference data of a glass plate. (b) depth profile. (c) xy-map of the 1st peaks location (top surface). (d) xy-map of the 2nd peaks location (bottom surface).

Lastly, subtracting depth position of the top surface with that of bottom surface yields the optical path length (OPL) of the light beam between the two surfaces. Dividing the OPL by the group index ($n = 1.5$) yields the thickness of a glass plate. By repeating the process for all A-scans across total 3D data set of a glass plate, the thickness map of a glass plate can be obtained by the difference between the positions of surface 1 and surface 2 as shown in Figure 3.9, so called thickness topography. Figure 3.9(a) and (b) are 3D surface plot and top view of the thickness topography result, respectively.

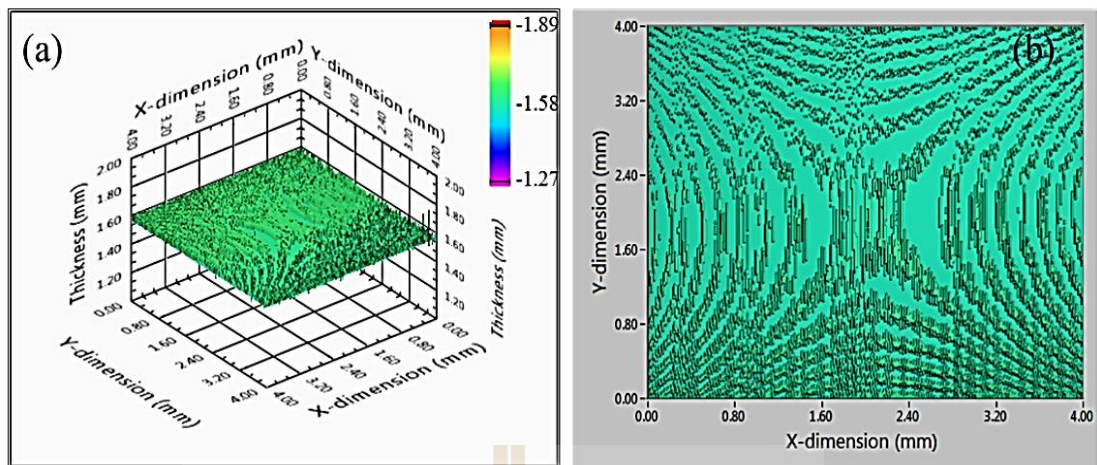


Figure 3.9 (a) xy-map OCT thickness topography of a glass plate. (b) top view OCT Thickness Topography in (a).

To confirm the accuracy of the developed system, the measurement result from OCT thickness topography was compared with that obtained by the digital micrometer as shown in Figure 3.10. The thickness of the same glass plate was measured across 50 different positions within the same region of interest as that of OCT topography.



Figure 3.10 Digital micrometer for measuring thickness of a glass plate.

Table 3.1 shows comparison of the measurement result of total thickness of a glass plate using digital micrometer and OCT topography technique. It shows that digital micrometer and optical topography technique measurements provide nearly the same value of the total thickness, but optical topography technique provides higher precision because its standard deviation (SD) was less than that of digital micrometer.

Table 3.1 Comparison of the measurement result of total thickness from digital micrometer and optical topography technique of a glass plate.

	Thickness in microns.	
	Average	SD
Digital micrometer (n=50)	156.34	1.89
OCT thickness topography	156.90	0.22

3.4 Sub-region thickness analysis

To quantify the thickness uniformity of the biofilm formation, we divided the surface area into multiple sub-regions and compute average thickness across each sub regions, which shows the thickness distribution and uniformity across the surface. For example, after obtaining the data of the thickness topography from previous methods as shown in Figure 3.11(a), we divide the surface area into 25 surfaces and compute the mean and standard deviation (SD) in each subregion to represent the thickness distribution and uniformity of a thin film as shown in Figure 3.11(b). Figure 3.11(c) is a map of the mean thickness of each sub-region, showing the thickness distribution across the surface of the thin film. Figure 3.11(d) is a map of the SD of the thickness of the thin film in each sub-region, representing the thickness uniformity of the sample. The multiple sub-regions thickness analysis method convenient for the non-uniformity sample since provided the value of thickness better than the conventional average value method. We can also plot the thickness topography 3D surface plot to see the uniformity of the growth of biofilm.

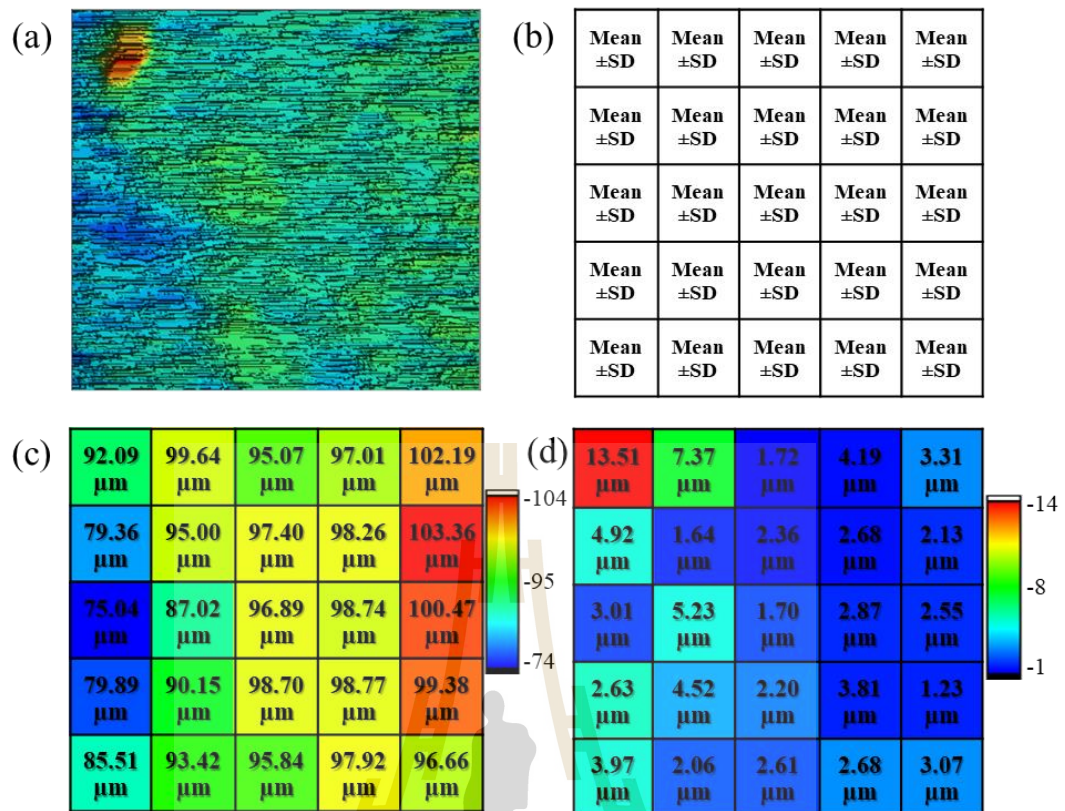


Figure 3.11 An illustration of sub-region thickness analysis. (a) OCT thickness topography obtain in section 3.3. (b) Example of 5×5 sub-region thickness analysis method by computing mean and SD in each sub-region. (c) A map of the mean thickness of each sub-region, showing the thickness distribution of the thin film. (d) A map of the SD of the thickness in each sub-region, showing the thickness uniformity of the thin film.

CHAPTER IV

RESULTS AND DISCUSSION

Figure 4.1(a-e) shows the top view of OCT image of the *L. pneumophila* biofilms pre-colonization on copper plate and after 7, 14, 21, and 28 days. Internal structures were observed by using OCT system. OCT images showed an increase in biofilm formation on the copper material structures. The images of internal material structures were processed by using ImageJ program. Image investigation was applied to quantify OCT images and monitor the change in the biofilm structure. Biofilm development was investigated over time with *L. pneumophila* cells operated. The variation in the meso-scale biofilm structure was monitored using OCT (Figure 4.1(a-e)). OCT image was taken with a clean plate followed by a continuous biofilm growth and the formation of structures. OCT images was confirmed with SEM on micro-scale as shown in Figure 4.1(f).

Figure 4.1(g-j) shows a set of 2D cross-sectional images of the *L. pneumophila* biofilm captured by OCT once a week for 4 weeks. It is clear from the figure that the thickness of the biofilm was not resolvable during the first two weeks (Figure 4.1(g) and (h)). Therefore, we only applied the algorithm of thickness topography to the 3D datasets of week 3 and week 4, i.e. Figure 4.1(i) and (j), respectively.

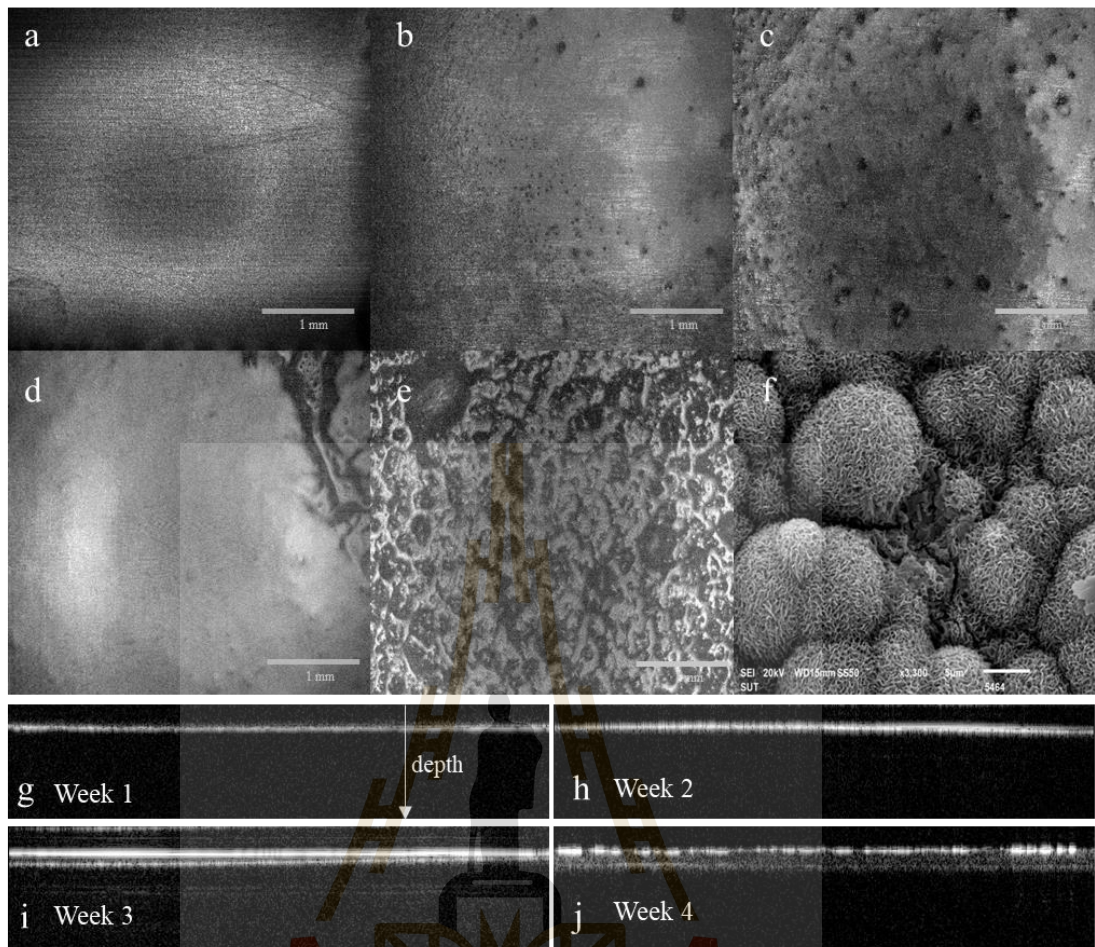


Figure 4.1 (a-e) Top view of OCT image developed on copper material (a. pre-colonization, b. day 7 c. day 14, d. day 21, e. day 28) bar scale is 1 mm and SEM on day 28 (f) bar scale is 10 μm , magnification 1300 \times and (g-j) is cross-sectional images of biofilm on copper surface in 4 weeks.

Figure 4.2(a) and (b) show surface topography of the top and the bottom interfaces, respectively, of the biofilm obtained at the 3rd week. Subtracting the locations of the top and bottom surfaces yields the optical thickness topography of the biofilm as shown by 3D surface plot in Figure 4.2(c) and top view of the topographic map in Figure 4.2(d). The total optical thickness and standard deviation of biofilm on copper surface at 3 weeks was computed to be $41.66 \pm 9.55 \mu\text{m}$.

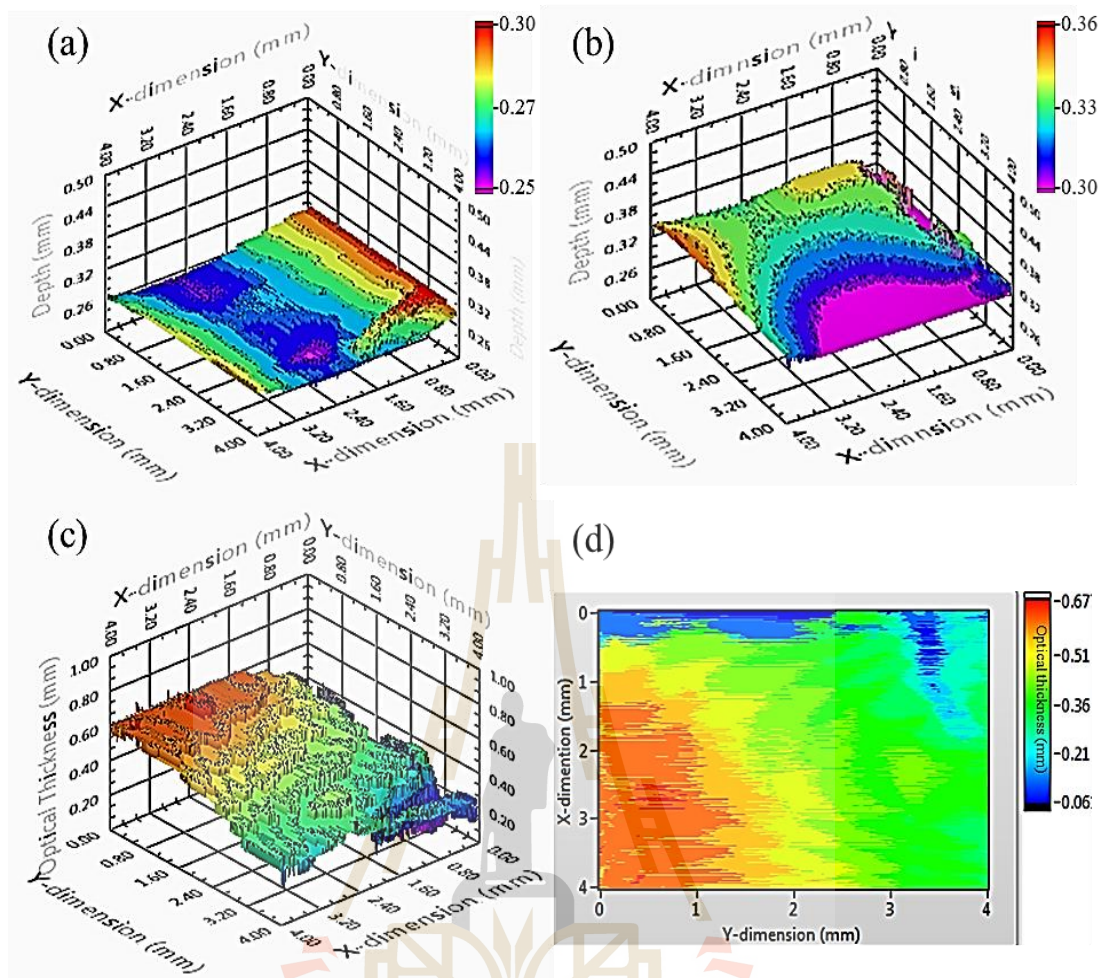


Figure 4.2 Biofilm in the 3rd week; (a) Top surface xy-map of peaks location and (b) Bottom surface xy-map of peaks location; (c) 3D surface plot of optical thickness topography of biofilm; (d) 2D map of the optical thickness topography of the biofilm.

Figure 4.3(a) and (b) show surface topography of the top and the bottom interfaces, respectively, of the biofilm obtained at the 4th week. Its 3D surface plot and 2D map of the optical thickness is shown in Figure 4.3(c) and (d), respectively. The total optical thickness and the standard deviation of the thickness was computed to be $94.15 \pm 3.17 \mu\text{m}$. The thickness of the biofilm dramatically increases from week 3 to week 4, revealing that *L. pneumophila* was rapidly growth during this period. Moreover, the SD is reduced by about half from week 3 to week 4, which implies that

the growth of the *L. Pneumophila* tended to uniformly spread out across the surface of the copper plate.

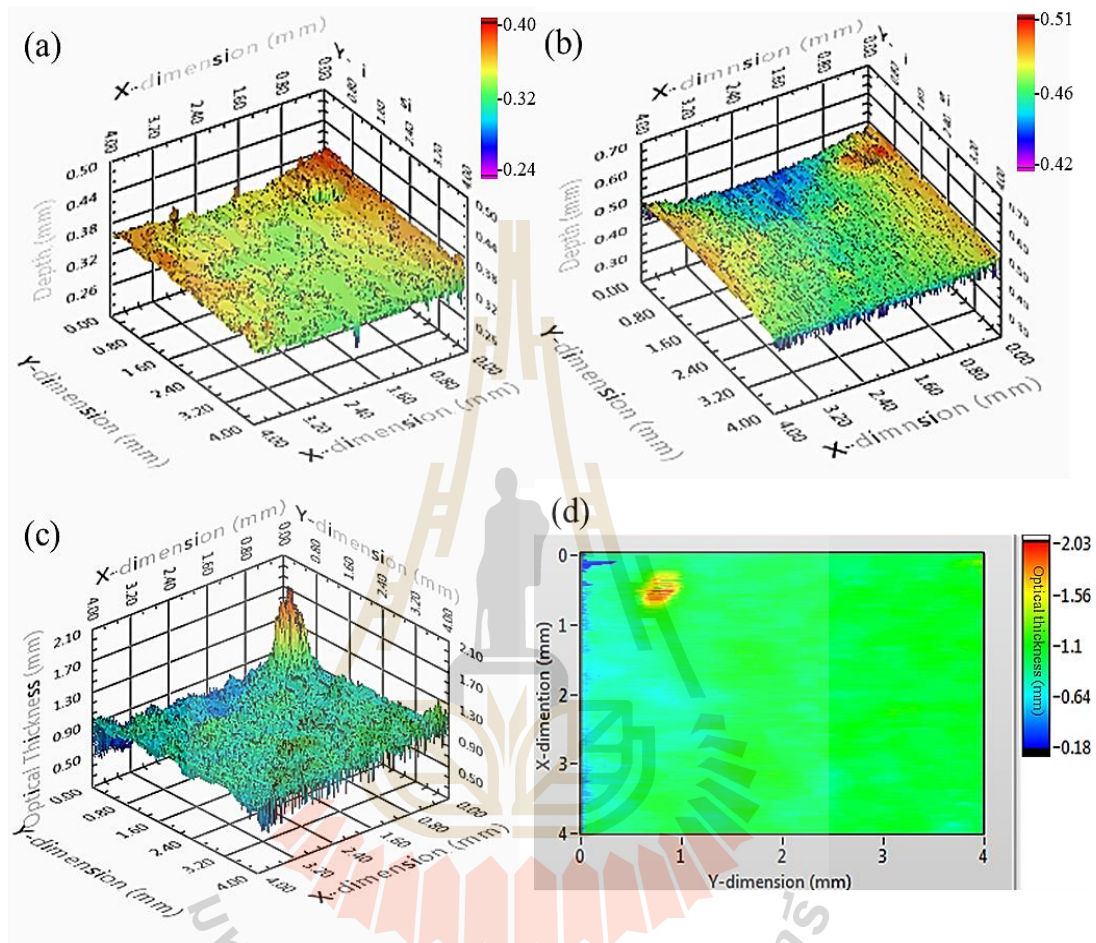


Figure 4.3 Biofilm in 4 weeks, Top surface xy-map of peaks location show in (a) and bottom surface xy-map of peaks location show in (b). Optical thickness topography of biofilm shows in (c) and (d) is top view of optical thickness topography.

Figure 4.4 shows *en face* images (top view) of the biofilm formation on the copper surface as captured by OCT. The two *en face* images were reconstructed from the 3D datasets obtained at week 3 (Figure 4.4(a)) and week 4 (Figure 4.4(b)). To quantify the thickness uniformity of the biofilm formation, we divided the surface area into 5×5 sub-regions (i.e. 100×100 pixels per sub-region) and computed the mean and

standard deviation of the optical thickness of the biofilm in each sub-region. It is clearly observable from Figure 4.4(a) and (b) that, besides the difference in thickness as previously shown in Figure 4.2 and Figure 4.3, the thickness distribution and uniformity across the surface is also different.

Furthermore, Figure 4.4(c) and (d) show color map of the mean thickness of biofilm in each sub-region of the 3rd week and the 4th week, respectively. The different increases in the thickness of biofilm formation at different sub-regions in each week are clearer observed. In addition, Figure 4.4(c) and (d) show color map of the SD of the thickness of biofilm in each sub-region of the 3rd week and the 4th week, respectively.

It should be noted that the number of sub-region can be increased at the expense of longer computation time to improve the visualization of the topographic map. Figure 4.5 shows sub-region thickness analysis by dividing the dataset into 50×50 sub-regions (i.e. 10×10 pixels per sub-region). Figure 4.5(a) and (b) show 3D surface plot of the sub-region analysis of the optical thickness of the biofilm in the 3rd week and 4th week, respectively. The 3D surface plots clearly show the difference of structure growth and biofilm formation between week 3 and week 4. The non-uniformity of the growth of the *L. Pneumophila* across the copper surface can be clearer observed as compared with the previous results.

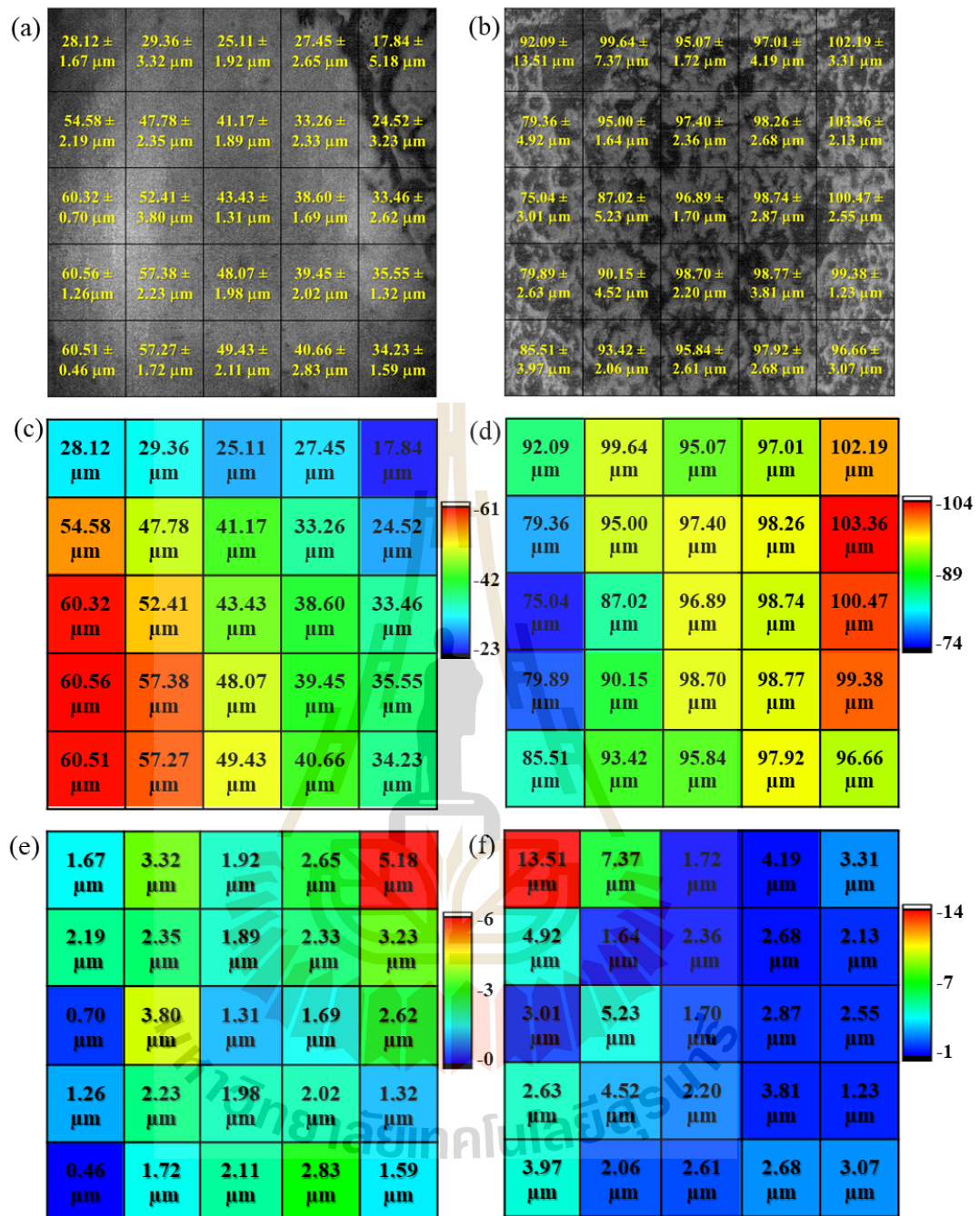


Figure 4.4 Sub-region optical thickness and its SD overlay on top of with *en face* OCT image of the biofilm during (a) 3 weeks and (b) 4 weeks of culture, respectively. A color map of the optical thickness of biofilm in week 3 and week 4 are shown in (c) and (d), respectively, (e) and (f) is a color map of the SD of the optical thickness of the biofilm in week3 and week4, respectively.

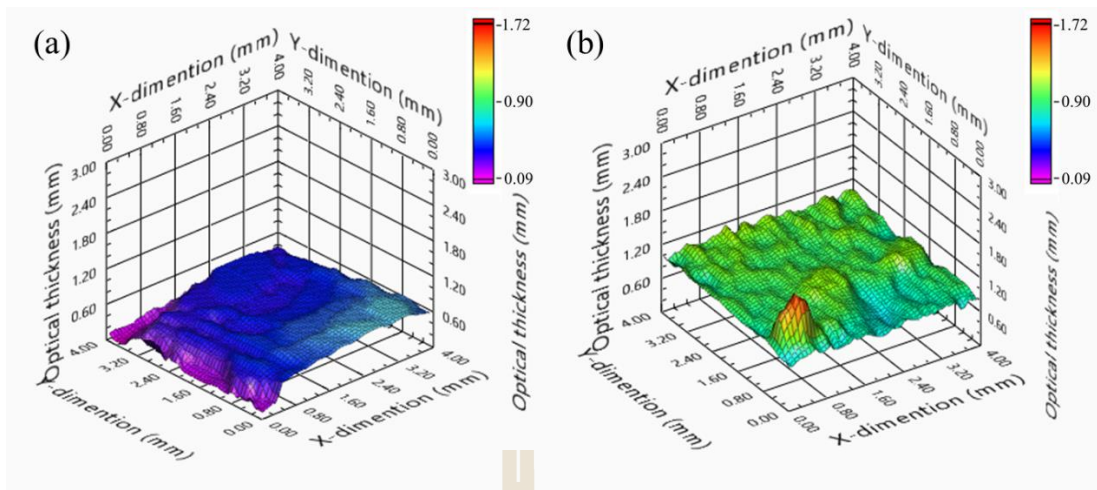


Figure 4.5 3D surface profiles of the sub-region thickness topography of the biofilm development in week 3 and week 4 are shown in (a) and (b), respectively.

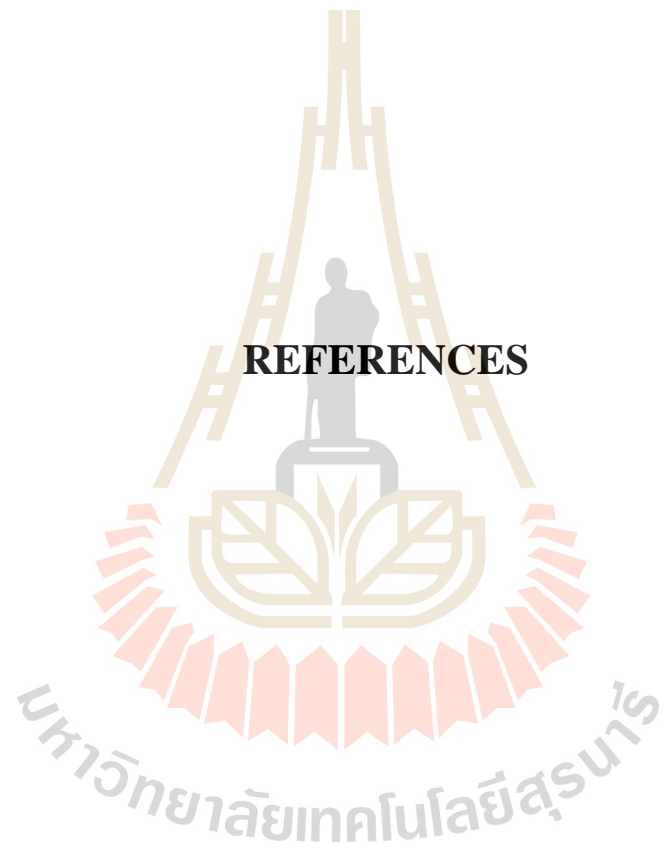
CHAPTER V

CONCLUSION

We have demonstrated the application of our custom developed 3D OCT imaging system to qualitatively and quantitatively monitor the development of biofilm formation on metal surface. In this work, the development of *L. pneumophila* biofilm on a copper surface was studied. The algorithm to extract the optical thickness topography from 3D OCT datasets has been developed and used to quantify the growth of *L. pneumophila* biofilm over a period of 4 weeks. The results show that OCT topography can detect visible internal structures in Legionella biofilm. It is proven to be useful for non-contact and non-destructive monitoring of biofilm development. It is confirmed that OCT can perform measurement of biofilm sample without the need to remove the cover plate of the chamber, which can prevent contamination for an experiment that requires environment control. Future studies should clarify chlorine treatment on the *L. pneumophila*. The information obtained by the developed OCT thickness topography would be useful for better understanding of treatment effects beyond viability calculation and treatment classification.

The developed procedure of OCT topography would be useful for medical diagnostics as well. As part of our future work, we aim to use the developed algorithm of the OCT topography to perform the thickness topography of human skin. We believe that the technique would be useful for quantitative evaluation of skin healthiness, such as monitoring of wound healing process, skin cosmetics and treatment, as well as extracting the dermal fingerprint for high security application.

REFERENCES



REFERENCES

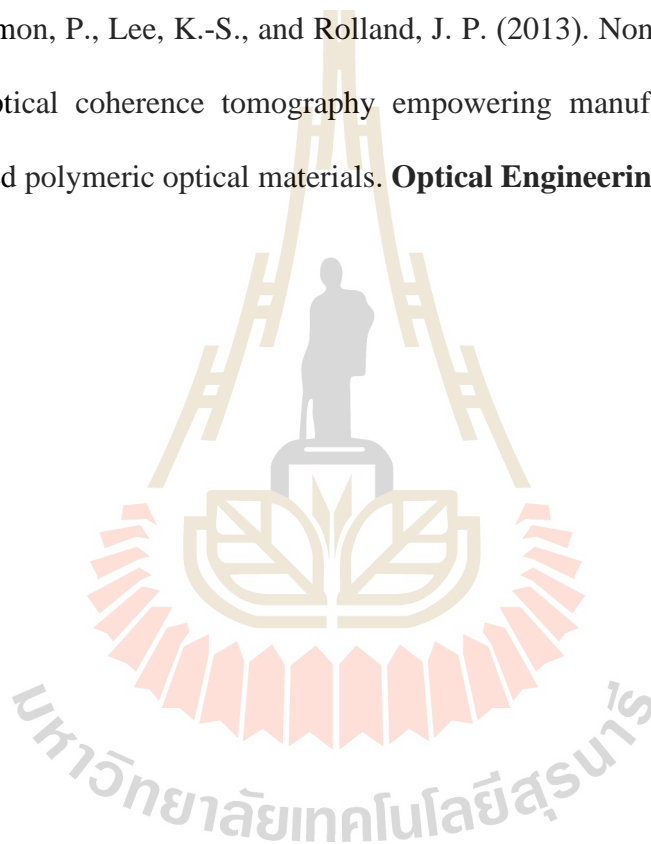
- Baer, E., Hiltner, P. A., and Shirk, J. S. (2006). Multilayer polymer gradient index (GRIN) lenses: Google Patents.
- Beyer, W. H. (1991). CRC standard mathematical tables and formulae. **Boca Raton, Fl.: Chemical Rubber Co., c1991, 29th ed., edited by Beyer, William H.**
- Born, M., and Wolf, E. (1999). Principles of Optics, seventh expanded edition. **Cambridge, England.**
- Cao, E., Chu, Z., Wang, H., Hao, W., Sun, L., and Zhang, Y. (2018). Effect of film thickness on the electrical and ethanol sensing characteristics of LaFeO₃ nanoparticle-based thick film sensors. **Ceramics International.** 44(6): 7180-7185.
- Collins, S., Stevenson, D., Bennett, A., and Walker, J. (2017). Occurrence of Legionella in UK household showers. **International journal of hygiene and environmental health.** 220(2): 401-406.
- Costa, J., da Costa, M. S., and Veríssimo, A. (2010). Colonization of a therapeutic spa with Legionella spp: a public health issue. **Research in microbiology.** 161(1): 18-25.
- Damodaran, V., Rao, S. R., and Vasa, N. J. (2016). Optical coherence tomography based imaging of dental demineralisation and cavity restoration in 840nm and 1310nm wavelength regions. **Optics and Lasers in Engineering.** 83: 59-65

- Debnath, S. K., Kothiyal, M. P., Schmit, J., and Hariharan, P. (2006). *Thickness-profile measurement of transparent thin-film layers by spectrally resolved phase-shifting interferometry*. Paper presented at the Interferometry XIII: Techniques and Analysis.
- Edelstein, P., Beer, K., Sturge, J., Watson, A., and Goldstein, L. (1985). Clinical utility of a monoclonal direct fluorescent reagent specific for *Legionella pneumophila*: comparative study with other reagents. **Journal of Clinical Microbiology**. 22(3): 419-421.
- Edelstein, P. H. (1981). Improved semiselective medium for isolation of *Legionella pneumophila* from contaminated clinical and environmental specimens. **Journal of Clinical Microbiology**. 14(3): 298-303.
- Fercher, F. A., Hitzenberger, C. K., Kamp, G., and El-Zaiat, S. Y. (1995). Measurement of intraocular distances by backscattering spectral interferometry. **Optics communications**. 117(1-2): 43-48.
- Fields, B. S., Benson, R. F., and Besser, R. E. (2002). *Legionella* and Legionnaires' disease: 25 years of investigation. **Clinical microbiology reviews**. 15(3): 506-526.
- Fortunato, L., Bucs, S., Linares, R. V., Cali, C., Vrouwenvelder, J. S., and Leiknes, T. (2017). Spatially-resolved in-situ quantification of biofouling using optical coherence tomography (OCT) and 3D image analysis in a spacer filled channel. **Journal of Membrane Science**. 524: 673-681.
- Haisch, C., and Niessner, R. (2007). Visualisation of transient processes in biofilms by optical coherence tomography. **water research**. 41(11): 2467-2472.

- Hee, M. R., Puliafito, C. A., Duker, J. S., Reichel, E., Coker, J. G., Wilkins, J. R., Schuman, J. S., Swanson, E. A., and Fujimoto, J. G. (1998). Topography of diabetic macular edema with optical coherence tomography. **Ophthalmology**. 105(2): 360-370.
- Horie, K., Shimada, Y., Matin, K., Ikeda, M., Sadr, A., Sumi, Y., and Tagami, J. (2016). Monitoring of cariogenic demineralization at the enamel–composite interface using swept-source optical coherence tomography. **Dental Materials**. 32(9): 1103-1112.
- Hsu, B.-M., Lin, C.-L., and Shih, F.-C. (2009). Survey of pathogenic free-living amoebae and Legionella spp. in mud spring recreation area. **water research**. 43(11): 2817-2828.
- Huang, D., Swanson, E. A., Lin, C. P., Schuman, J. S., Stinson, W. G., Chang, W., Hee, M. R., Flotte, T., Gregory, K., and Puliafito, C. A. (1991). Optical coherence tomography. **Science (New York, NY)**. 254(5035): 1178.
- Kim, S.-H., Kim, J.-H., and Kang, S.-W. (2011). Nondestructive defect inspection for LCDs using optical coherence tomography. **Displays**. 32(5): 325-329.
- Kim, S.-W., and Kim, G.-H. (1999). Thickness-profile measurement of transparent thin-film layers by white-light scanning interferometry. **Applied Optics**. 38(28): 5968-5973.
- Kim, Y. G., Seo, Y. B., and Joo, K.-N. (2013). Low cost wafer metrology using a NIR low coherence interferometry. **Optics express**. 21(11): 13648-13655.
- Meemon, P., Yao, J., Lee, K.-S., Thompson, K. P., Ponting, M., Baer, E., and Rolland, J. P. (2013). Optical coherence tomography enabling non destructive metrology of layered polymeric GRIN material. **Scientific reports**. 3: 1709.

- Meemon, P., Yao, J., and Rolland, J. P. (2014). *Design consideration and performance analysis of OCT-based topography*. Paper presented at the Optical Coherence Tomography and Coherence Domain Optical Methods in Biomedicine XVIII.
- Napoli, C., Iatta, R., Fasano, F., Marsico, T., and Montagna, M. T. (2009). Variable bacterial load of *Legionella* spp. in a hospital water system. **Science of the total environment**. 408(2): 242-244.
- Qin, Y., Zhao, H., Zhang, L., and Wang, L. (2013). Film thickness measurement and defect inspection using optical coherence tomography. **Optik - International Journal for Light and Electron Optics**. 124(22): 5293-5296.
- Roig, J., Aguilar, X., Ruiz, J., Domingo, C., Mesalles, E., Manterola, J., and Morera, J. (1991). Comparative study of *Legionella pneumophila* and other nosocomial-acquired pneumonias. **Chest**. 99(2): 344-350.
- Rothen, A. (1945). The ellipsometer, an apparatus to measure thicknesses of thin surface films. **Review of Scientific Instruments**. 16(2): 26-30.
- Steinert, M., Hentschel, U., and Hacker, J. (2002). *Legionella pneumophila*: an aquatic microbe goes astray. **FEMS microbiology reviews**. 26(2): 149-162.
- Sun, M., Birkenfeld, J., de Castro, A., Ortiz, S., and Marcos, S. (2014). OCT 3-D surface topography of isolated human crystalline lenses. **Biomedical optics express**. 5(10): 3547-3561.
- Weiss, N., El Obied, K. E. T., Kalkman, J., Lammertink, R. G., and van Leeuwen, T. G. (2016). Measurement of biofilm growth and local hydrodynamics using optical coherence tomography. **Biomedical optics express**. 7(9): 3508-3518.

- Xi, C., Marks, D., Schlachter, S., Luo, W., and Boppart, S. A. (2006). High-resolution three-dimensional imaging of biofilm development using optical coherence tomography. **Journal of biomedical optics**. 11(3): 034001-034001-034006.
- Xu, Q., Ye, Y., Chen, V., and Wen, X. (2015). Evaluation of fouling formation and evolution on hollow fibre membrane: Effects of ageing and chemical exposure on biofoulant. **water research**. 68: 182-193.
- Yao, J., Meemon, P., Lee, K.-S., and Rolland, J. P. (2013). Nondestructive metrology by optical coherence tomography empowering manufacturing iterations of layered polymeric optical materials. **Optical Engineering**. 52(11): 112111.



CURRICULUM VITAE

Name Mr. Jadsada Saetiew

Date of Birth 23 August 1991

Place of Birth Phayao, Thailand

Education

- 6 March 2014, Bachelor Degree of Science in Physics, UNIVERSITY OF PHAYAO.

Publications

- Saetiew, J., Meemon, P., Ritpech, S., and Saovana, T. (2017). Optical topography technique for characterization and monitoring of biofilm thickness uniformity. In 2017 10th Biomedical Engineering International Conference (BMEiCON) (pp. 1-5). IEEE.

Awards

- Panomsak Meemon, Jadsada Saetiew, Jiraporn Saenjae. Infrared Microscope for non-contact thin film thickness topography. 3st runner-up Award, Innovation and Technology Exposition 2018.
- Panomsak Meemon, Kunakorn Palawong, Racha Pongchalee, Jadsada Saetiew, Jiraporn Saenjae. High-speed infrared microscope for nondestructive 3D cross-sectional imaging of biological samples. Excellent Award, Innovation and Technology Exposition 2015.